Unified Electromagnetic Theory of Matter and Light

Section D — **Structure and Dynamics of the Universe**

Part D1 - Pulsar Pulses from Magnetospheric Resonance

Franc Rozman

Abstract

This study develops an alternative model of pulsar emission in which the repetition of electromagnetic pulses is governed primarily by a global resonance of the neutron-star magnetosphere rather than necessarily by rapid stellar rotation. A simplified inductive–capacitive (LC) representation is used to estimate characteristic oscillation frequencies, while spatially distributed magnetohydrodynamic motions describe the possible deformation of emitting regions. Irregular disturbances originating in the star and its environment are considered as a source of excitation, with the distinction between resonance selection and long-term phase coherence explicitly maintained. The proposed radiation mechanism assumes a source-velocity-dependent propagation law, c + u, and examines how variations in the velocities of continuously emitting magnetospheric regions could alter the mapping from emission time to arrival time at a distant observer. A five-region numerical example produces a strongly modulated light curve along the oscillation axis, with a peak approximately eight times the mean intensity and a pulse width of about 0.86 ms for an assumed 33.5 ms period; the modulation diminishes with viewing angle and vanishes in the transverse direction in this idealized configuration. Two regions coupled to the same global oscillation can produce a double-peaked profile, although their relative phase is prescribed rather than derived from magnetospheric dynamics. The Crab pulsar is used as a comparative case for pulse timing, observed flux, spectral differences, and polarization. The analysis demonstrates the internal mathematical behavior of the proposed model but does not independently establish a physical LC eigenmode, the required magnetospheric velocity distribution, or the assumed propagation law. Laboratory tests proposed separately for the latter, together with quantitative predictions for pulse phase and viewing geometry, provide routes for discriminating this hypothesis from the established rotational interpretation.

Keywords: *pulsars; neutron-star magnetosphere; electromagnetic resonance; LC model; temporal concentration; source-dependent propagation; pulse profiles*

1. Introduction

1.1. Observed Properties of Pulsars

Pulsars are among the most remarkable sources of periodic electromagnetic radiation observed in the universe. Their defining characteristic is the repetition of radiation pulses at exceptionally stable intervals, ranging from milliseconds to several seconds or longer. In some objects, the regularity of these intervals allows the arrival times of successive pulses to be predicted with extraordinary precision.

Despite this temporal regularity, pulsars exhibit considerable diversity in their radiation profiles. Some produce narrow, intense pulses occupying only a small fraction of the repetition period, whereas others exhibit broad emission profiles extending over a substantial part of the cycle. In certain pulsars, electromagnetic radiation remains detectable throughout nearly the entire period, with only relatively small variations in intensity.

The observed pulse profiles may contain one, two, or several distinct intensity maxima. These components can differ in amplitude, duration, and temporal separation. Although individual pulses may exhibit considerable fluctuations, the average profile obtained from many successive cycles is often remarkably stable. This combination of long-term periodicity and short-term variability is an important observational characteristic of pulsar emission.

Pulsars also exhibit diverse spectral properties. While many are predominantly observed at radio frequencies, some emit detectable radiation across much broader spectral ranges, including visible light, X-rays, and gamma rays. The relative intensities, widths, and phases of individual pulse components may vary with electromagnetic frequency. Consequently, different spectral bands do not necessarily display identical pulse profiles.

Polarization measurements provide additional information about the emitting regions. Radio pulses frequently exhibit significant linear or circular polarization, while the polarization position angle may vary across the observed profile. Different pulse components can also display different polarization characteristics, indicating differences in the electromagnetic conditions or geometry associated with their emission.

An additional observational consideration is the dependence of pulsar detection on the direction of observation. Electromagnetic radiation need not be distributed uniformly over all directions, and the radiation profile detected by a particular observer represents only the signal arriving along that line of sight. The observed intensity, pulse width, and number of distinguishable components therefore provide incomplete information about the total radiation emitted by the source.

These observations establish the principal physical quantities that any proposed pulsar mechanism must address: the stability of the repetition period, the formation of narrow and broad intensity profiles, the occurrence of multiple pulse components, and the spectral and polarization properties of the received radiation. They also motivate a distinction between the intrinsic electromagnetic activity of the source and the temporal distribution of radiation received by a distant observer. **[1, 2]**

1.2. The Conventional Rotational Interpretation

The conventional interpretation identifies a pulsar as a rotating, strongly magnetized neutron star. Its magnetic axis may be inclined relative to the rotation axis, allowing radiation associated with the magnetosphere to sweep across the observer's line of sight. In this interpretation, the observed repetition period generally reflects the stellar rotation period, or a related harmonic of it. The pulse profile is governed by the geometry and physical conditions of the emitting regions.

This rotational picture is supported by several independent observational results, including periodic signals from accreting neutron stars, characteristic changes in pulse arrival times, and polarization patterns associated with the magnetic-field geometry. The model also links the gradual increase in the periods of many isolated pulsars to the loss of rotational energy, although the detailed mechanisms responsible for coherent radio emission remain under investigation.

Nevertheless, periodic radiation and rotation are distinct physical quantities. Observing a stable pulse period establishes a regular modulation of the received signal; interpreting that period as the stellar rotation period requires a physical model. This distinction motivates an investigation of whether a magnetosphere could generate periodic radiation through an electromagnetic resonant process, even when the star itself rotates slowly.

The present study does not assume that neutron stars cannot rotate, nor does it dismiss the observational evidence supporting rotational pulsar models. Instead, it develops a specific alternative hypothesis in which the primary pulse periodicity is associated with a global mode of magnetospheric oscillation. **[2]**

1.3. Motivation for a Resonant Magnetospheric Model

A neutron-star magnetosphere is an extended electromagnetic system containing strong magnetic fields, electric currents, charged particles, and plasma. It can support disturbances and oscillatory modes whose spatial scales are much larger than the stellar radius. The possibility that a global electromagnetic mode may establish a characteristic repetition frequency provides the starting point for the present model.

In a simplified representation, the magnetospheric current system contributes an effective inductance, while the separation of electric charge and the associated electric-field energy contribute an effective capacitance. Their coupling suggests an LC-type resonance. The actual magnetosphere is a distributed plasma system rather than an ordinary circuit, so this representation is treated as an approximation. Local magnetohydrodynamic motions and irregular electromagnetic disturbances may excite the global mode and contribute to variations in its amplitude and spatial structure.

The proposed mechanism distinguishes intrinsic emission from the time distribution of radiation received by a distant observer. Different magnetospheric regions are assumed to emit radiation continuously or intermittently in directions that include the observer. A spatially and temporally varying velocity field can then affect the mapping between emission time and arrival time under the propagation hypothesis adopted in this study. Suitable configurations may concentrate the received radiation into short intervals, whereas other configurations may produce broad pulses or weak modulation.

This arrival-time mechanism depends on the proposed source-velocity-dependent propagation relation, written schematically as c + u, with u denoting the appropriate line-of-sight source velocity. That relation is not a prediction of established vacuum electrodynamics, in which light propagates at c independently of the source velocity. The companion study Part C2 proposes differential measurements intended to test the alternative relation directly. The two investigations are therefore complementary: the laboratory-scale test addresses the propagation premise, while the present paper examines its conditional astrophysical consequences. [18]

Within this framework, the observed pulse period need not be identified with a rapid stellar rotation. A slowly rotating or nonrotating star provides the simplest initial geometry. Rotation, binary motion, and variations in magnetospheric conditions may

subsequently be considered as additional influences on the observed signal.

1.4. Scope and Objectives of the Study

The objective of this paper is to formulate and quantitatively examine a resonant magnetospheric mechanism for periodic electromagnetic pulses. The analysis first introduces an approximate electromagnetic-resonator description of the magnetosphere and relates its characteristic frequency to the assumed current paths, electric-field structure, and spatial scale. It then considers the excitation of global oscillations by irregular disturbances and their coupling to local plasma motion.

A three-dimensional description is used to distinguish the spatial distribution of magnetospheric velocities from their temporal evolution. The resulting arrival-time mapping is applied to continuously emitting regions to calculate illustrative light curves for observers viewing the same source from different directions. The model also considers the possibility that two separated active regions, for example in northern and southern portions of the magnetosphere, produce distinct components within one resonant cycle.

The calculations are compared with selected observational characteristics of the Crab pulsar, including its repetition period, radio flux, pulse profile, and the spectral and polarization differences between its principal components. Such comparisons are used to identify consistency conditions and testable predictions; parameters chosen to reproduce an observed value are not presented as independent predictions.

The scope is deliberately limited. The proposed propagation law and the existence of a sufficiently coherent global LC-like mode remain hypotheses requiring independent verification. The study does not attempt a complete plasma-kinetic description of broadband emission, nor does it claim that arrival-time concentration alone determines the emitted spectrum or supplies the radiated energy. Its primary aim is to establish a transparent mathematical framework and identify observations capable of distinguishing the proposed mechanism from the conventional rotational interpretation.

2. Physical Foundations of the Proposed Model

The proposed mechanism combines the dynamics of an extended neutron-star magnetosphere with a specific hypothesis about the propagation of radiation emitted by moving source regions. The two elements must be distinguished. Electromagnetic and magnetohydrodynamic oscillations are well-established physical possibilities in magnetized plasmas, whereas the source-velocity-dependent propagation law used below is a separate, experimentally unconfirmed premise. The purpose of this chapter is to state these foundations precisely before introducing resonance calculations and predicted pulse profiles.

2.1. The Neutron Star and Its Magnetosphere

A neutron star is a compact object with an extremely strong gravitational field and, in many cases, a strong magnetic field. Surrounding it is a magnetosphere: an extended region containing electromagnetic fields, charged particles, and electric currents. Its structure is not fixed solely by the surface magnetic field. Plasma motion, charge separation, current closure, and the exchange of energy with the star and its environment also influence the field configuration.

For the initial model, the stellar radius is denoted by R* and the characteristic radial extent of the resonant magnetospheric region by R_m. These quantities should not be confused. A representative stellar radius of 12 km may be used while the candidate oscillating

region extends hundreds or thousands of kilometres from the stellar centre. Such dimensions are model parameters and are not assumed to describe a uniquely established resonant boundary.

The simplest reference geometry is approximately axisymmetric about a magnetic axis. Local disturbances may alter this symmetry, while a slowly rotating star can introduce additional transverse motions and phase-dependent distortions. Stellar rotation is not required as the clock that determines pulse repetition in the proposed mechanism; the consequences of nonzero rotation are examined separately in Chapter 10.

A particularly useful candidate oscillation is a global deformation in which an increase in equatorial extent accompanies a decrease in polar extent. This motion is analogous to a quadrupolar mode, but the actual magnetosphere is not a solid membrane with a sharply defined outer surface. Any admissible deformation must obey the electromagnetic and plasma-dynamical equations and the appropriate boundary conditions at the stellar surface. **[3]**

2.2. Electromagnetic Radiation from Magnetospheric Plasma

The model distinguishes the production of radiation from its subsequent reception by an observer. Magnetospheric plasma may generate radiation through several processes associated with accelerated charges, collective plasma motion, and electromagnetic instabilities. The resulting spectral distribution need not resemble the approximately thermal emission of the neutron-star surface. In particular, pulsed radio emission is commonly associated with coherent processes, whereas high-energy emission involves different particle and radiation mechanisms.

To isolate the proposed arrival-time mechanism, the first calculation treats a number of source elements as emitting continuously with prescribed power. Each element is assumed to contribute radiation along the line of sight toward a distant observer. An isotropic angular emission pattern may be adopted as a mathematical simplification; actual magnetospheric radiation can be strongly anisotropic, polarized, and frequency dependent. The observer consequently receives only the portion of the local emission directed along the relevant ray path.

Emission from distinct source elements is initially added as an incoherent sum of energy fluxes. This avoids assuming a fixed phase relationship between the electromagnetic carrier waves emitted by spatially separated regions. A separate phase-coherent treatment would be required to investigate interference. The repetition frequency of a magnetospheric oscillation must also be distinguished from the much higher carrier frequencies of radio, optical, X-ray, or gamma-ray radiation.

An active region may occupy one contiguous part of the magnetosphere. Its total emitting area, rather than the number of smaller mathematical elements used to represent it, determines the amount of radiation available for a pulse at fixed surface emissivity. Neither a fixed emitting area nor a fixed pulse width is imposed universally: both may differ between objects, observation directions, and spectral bands.

2.3. Source Motion and the Proposed Propagation Law c + u

A central premise of the present model is that the velocity of a radiating source region may affect the propagation speed assigned to its emitted electromagnetic radiation in the observer frame. In the notation used here, u is the component of source velocity toward the observer, and the proposed effective speed is written as

$$v_{\mathrm{prop}} = c + u$$

This relation is a hypothesis developed in Part C2 of the accompanying series, which proposes

laboratory-scale differential tests of source-motion effects. Those proposed tests offer a possible empirical route to evaluating the premise, but a test proposal is not evidence that the relation has already been established. The relation differs from the prediction of standard special-relativistic electrodynamics for freely propagating light in vacuum, where the measured local speed is c independent of source velocity. [18]

For a source element indexed by i, let t_e be the emission time, $r_i(t_e)$ its location, and r_O the position of a distant observer. Its geometric path length is

$$L_i(t_e) = |\mathbf{r}_O - \mathbf{r}_i(t_e)|$$

In the model, if the effective propagation speed remains $c + u_i(t_e)$ during travel, the arrival-time mapping is

$$t_{a,i}(t_e) = t_e + \frac{L_i(t_e)}{c + u_i(t_e)}$$

This equation is used as a kinematic definition for the calculations that follow. It is not derived from the Maxwell equations in vacuum. Effects of propagation through intervening plasma and other media are excluded from the first approximation and may be included as additional delays when required.

The distinction between a spatially varying velocity field and a time-varying one is essential. A distribution of u across the magnetosphere may equalize propagation delays between different source elements at a given emission time. Time variation of u, however, determines whether radiation emitted at successive times becomes compressed or expanded in the received time coordinate.

2.4. Spatial and Temporal Concentration of Radiation

Consider a source region parameterized by a spatial coordinate s. The corresponding arrival-time function is

$$t_a(s, t_e) = t_e + \frac{L(s, t_e)}{c + u(s, t_e)}$$

Spatial synchronization means that radiation emitted from an extended part of the source at approximately the same instant reaches the observer within a narrow arrival-time interval. Its local mathematical condition is

$$\left.\frac{\partial t_a}{\partial s}\right|_{t_e} \approx 0$$

The spatial condition alone does not imply a bright pulse from a continuously radiating source. If the emission from all regions is already steady, merely making their travel times equal leaves the time-averaged received flux unchanged. A distinct mechanism is needed to create temporal variation in the arrival rate of emitted energy.

Temporal concentration instead refers to compression of the interval between radiation emitted at successive times. It is governed by the derivative of the arrival-time mapping at fixed source position label:

$$J(s, t_e) = \frac{\partial t_a(s, t_e)}{\partial t_e}$$

When J is small, a finite emission interval can be mapped into a shorter reception interval in the proposed model. For a monotonic arrival-time branch and a locally conserved energy contribution, the received flux is inversely proportional to J. A schematic expression for an unresolved source is

$$F(t_a) = \int_S \sum_{k \in \mathcal{B}(s,t_a)} \frac{j(s, t_{e,k})}{|J(s, t_{e,k})|}\, \mathrm{d}S$$

where j includes emitted power per unit area, geometric dilution, and the appropriate angular contribution. Each term is evaluated at an emission time that maps to the observed t_a. If multiple emission times map to the same arrival time, the branch contributions must be added. Near J = 0 the idealized expression can become singular; finite emitting volumes,

bandwidth, time resolution, and other physical effects must regularize any realistic prediction.

The spatial and temporal aspects can therefore coexist without being identical. The spatial extent of the contributing region controls the available energy, while the time mapping controls its distribution among reception intervals. The oscillation amplitude enters through the velocity field u(s,t); it does not, by itself, uniquely determine the pulse brightness. An explicit source-power model and a specified velocity distribution are both required.

The effect is observer dependent. The line-of-sight velocity component and geometrical path differences vary with viewing direction, so the same oscillating magnetosphere could, under the proposed law, produce a narrow high-contrast profile in one direction, a broad weakly modulated profile in another, and a nearly constant profile elsewhere. Chapter 7 tests this consequence using a prescribed sinusoidal velocity field.

2.5. Principal Assumptions and Model Limitations

The theoretical construction is deliberately modular. The following assumptions define the scope of the quantitative examples and indicate which aspects require independent justification:

- Global resonance: a sufficiently coherent electromagnetic or electromagnetic–plasma mode exists within an extended region of the magnetosphere. An equivalent LC representation is used as an initial approximation, not as proof of a physically isolated spherical capacitor or a single lumped current loop.
- Excitation: irregular activity in the star and its surroundings can supply energy to the resonant mode. Whether the resulting phase coherence is adequate for observed pulsar timing precision remains an open dynamical problem.
- Propagation: source radial velocity enters the postulated observer-frame propagation speed as c + u. This premise differs from accepted vacuum electrodynamics and must be evaluated experimentally, independently of the pulsar interpretation.
- Emission: the source elements emit with prescribed power, and their incoherent energy-flux contributions are added. Detailed radiation-generation physics, spectral transfer, and polarization are not derived from the LC approximation.
- Geometry: a simple active region and a prescribed oscillation field are used before treating a realistic three-dimensional plasma configuration. Both spatial coincidence and time compression are tracked; neither is silently substituted for the other.
- Validation: agreement obtained by selecting an effective magnetospheric size to reproduce an observed period is parameter matching, not an independent prediction. Quantitative tests must additionally examine observed profile shape, brightness, frequency dependence, phase stability, and the energetic environment.

Within these limits, the paper develops a testable conditional model: if the proposed propagation law holds and a suitable global magnetospheric mode exists, can a physically specified velocity field transform continuous radiation into the observed pulse profiles? The next chapters address the candidate resonant structure, its excitation, the spatial dynamics of the magnetosphere, and the resulting arrival-time calculations. The comparison with a real pulsar is used to identify both potential consistency and discrepancies rather than to claim confirmation from a fitted period alone.

3. Global Electromagnetic Resonance of the Magnetosphere

The proposed model treats the magnetosphere of a neutron star as a spatially extended electromagnetic resonator. Its large-scale currents store magnetic energy, while charge separation and electric-field configurations store electric energy. The exchange between these contributions provides a possible mechanism for a preferred oscillation frequency. The purpose of this chapter is to obtain a transparent geometric estimate and then identify the conditions under which it can represent a physical eigenmode of the magnetosphere.

The inductance and capacitance used below belong to an equivalent-circuit approximation. The actual magnetosphere is a distributed, strongly magnetized plasma with no rigid outer electrode or prescribed wire path. Consequently, agreement between an LC frequency and an observed pulse repetition frequency is a numerical consistency check, not an independent derivation of pulsar timing.

3.1. Magnetospheric Inductance

A closed current path with characteristic radius R and effective current-channel radius a may be approximated by a thin circular loop. Its low-frequency external self-inductance is

$$L \approx \mu_0 R[\ln(\frac{8R}{a}) - 2].$$

This formula assumes a single approximately circular conducting path, a/R much smaller than unity, and a current distribution for which the external magnetic flux dominates the inductance. In a magnetosphere, the effective current channel may differ substantially from a circular wire; the calculated L must therefore be interpreted as a geometric estimate [4, 5].

For illustration, adopt the relative channel radius a/R = 0.01. The logarithmic factor is then independent of R:

$$L(R) \approx \mu_0 R[\ln(800) - 2] \approx 5.887 \times 10^{-6}\, R \text{ H},$$

R is expressed in metres in the last expression. **[4], [5]**

3.2. Effective Spherical Capacitance

A complementary geometric estimate represents the neutron-star surface as an inner spherical electrode of radius R_0 and a hypothetical equipotential shell of radius R as the outer electrode. In a vacuum, the capacitance of two concentric spheres is

$$C(R) = 4\pi\varepsilon_0 \frac{R_0 R}{R - R_0}.$$

For R_0 = 12 km and R = 1000 km this expression gives C = 1.351 µF. Since R is much greater than R_0, the capacitance approaches the isolated-sphere value:

$$C(R) \approx 4\pi\varepsilon_0 R_0 \ (R \gg R_0).$$

The outer shell is a mathematical boundary, not an assumed solid structure in the magnetosphere. A plasma may screen electrostatic fields, develop field-aligned currents, and depart strongly from spherical equipotential geometry. The actual effective capacitance must therefore be defined from the perturbation electric energy and a physically identifiable potential difference, rather than inferred from the dimensions alone.

3.3. Natural Frequency of the Equivalent LC Resonator

In a lossless lumped-element approximation, the electric charge Q on the effective capacitance satisfies

$$L\frac{d^2Q}{dt^2} + \frac{Q}{C} = 0.$$

Its characteristic angular frequency and period are

$$\omega_0 = \frac{1}{\sqrt{LC}}; \quad f_0 = \frac{1}{2\pi\sqrt{(LC)}}; \quad T_0 = 2\pi\sqrt{(LC)}.$$

At R = 1000 km, using the same channel ratio a/R = 0.01 and R_o = 12 km, the equivalent values are:

Quantity	Geometric estimate
Loop inductance, L	5.887 H
Spherical capacitance, C	1.351 μF
Frequency, f_o	56.43 Hz
Period, T_o	17.72 ms

These values follow from chosen dimensions without setting C to reproduce a target frequency. Nevertheless, they do not establish the existence of the corresponding physical resonant mode: a current-closure path and an electric-field pattern that couple dynamically must be specified.

3.4. Dependence of Resonance on Magnetospheric Dimensions

Keeping the stellar radius and channel aspect ratio fixed, the capacitance changes only weakly once R becomes much larger than R_o, while the inductance grows nearly in proportion to R. The equivalent-circuit period therefore behaves approximately as

$$L \propto R, \quad C \approx \text{constant}, \quad T_0 \propto \sqrt{R}, \quad f_0 \propto \frac{1}{\sqrt{R}}.$$

Table 1 gives numerical values for a representative range of loop radii.

R (km)	L (H)	C (μF)	f_o (Hz)	T_o (ms)
100	0.589	1.517	168.40	5.94
250	1.472	1.403	110.78	9.03
500	2.943	1.368	79.31	12.61
1,000	5.887	1.351	56.43	17.72
1,500	8.830	1.346	46.17	21.66
3,000	17.661	1.341	32.71	30.57
3,605	21.222	1.340	29.85	33.50

Table 1. Geometrical LC estimates for R_o = 12 km and a/R = 0.01. The last row illustrates the value of R that reproduces approximately 33.5 ms, but R is fitted rather than independently measured.

For example, the 33.5 ms repetition period commonly used as a reference for the Crab pulsar corresponds in this idealized model to R ≈ 3605 km. This correspondence is not a prediction: it results from solving the assumed LC formula for R. A meaningful observational test would require an independent determination of the characteristic resonant radius or of the magnetospheric eigenfrequency.

3.5. Distributed Electromagnetic Resonance and Standing Waves

The key limitation of the lumped LC picture is the finite propagation speed of disturbances. For a circular path of radius R, the shortest vacuum travel time for a disturbance to complete one circumference is

$$t_{circ} = \frac{2\pi R}{c}.$$

At R = 1000 km, t_circ = 20.96 ms, compared with the estimated LC period T_o = 17.72 ms. At R = 3605 km, the corresponding times are 75.56 ms and 33.50 ms. A single phase shared instantaneously by all parts of the path is thus not a reliable approximation. A distributed-field description becomes necessary; a wave mode may still exist, but its eigenfrequency is determined by its geometry, wave propagation, coupling and boundary conditions.

For an idealized standing disturbance on a path of length ℓ, with wave speed v and boundary conditions appropriate to two nodes, a fundamental estimate is

$$f_1 \approx \frac{v}{2\ell}.$$

For v ≈ c, a length ℓ ≈ 3000 km corresponds to f_1 ≈ 50 Hz. In the real magnetosphere, Alfvénic and fast magnetosonic disturbances can be coupled and have different spatial patterns. A recent force-free treatment explicitly calculates normal modes in dipolar neutron-star magnetospheres and demonstrates their coupling [6]. This supports investigation of distributed resonance, without validating the particular spherical-capacitor/circular-loop equivalent circuit.

For the proposed model, the global resonance is therefore best represented as an

electromagnetic eigenmode whose energy may be described approximately by effective L and C. Local deformation of the plasma, including equatorial expansion and polar contraction, may be a coupled dynamical response rather than identical to the global circuit coordinate. **[6]**

3.6. Energy Exchange Between Electric and Magnetic Fields

In the ideal LC analogy, the total perturbation energy alternates between the electric and magnetic contributions:

$$W_E = \frac{1}{2}CU^2, \quad W_B = \frac{1}{2}LI^2.$$

$$W_{mode} = W_E + W_B = \text{constant} \quad \text{(ideal lossless case)}.$$

For a spatially distributed magnetosphere, the corresponding field energies must be defined from the oscillatory electric and magnetic perturbations over the relevant volume. One useful linearized expression is

$$W_{mode} \approx \frac{1}{2}\int_V \left[\varepsilon_0(\delta E \cdot \delta E) + \frac{(\delta B \cdot \delta B)}{\mu_0}\right] dV,$$

with appropriate additional plasma kinetic and interaction terms when the medium is dynamical. The large energy stored in the stationary background dipole field must not be equated with the energy of the oscillation itself.

Real modes are damped by radiation, plasma processes and redistribution of energy into other modes. An effective quality factor may be introduced by the energy-loss relation

$$P_{loss} \approx \frac{\omega_0 W}{Q}.$$

Random electromagnetic disturbances generated by the star and its surroundings may replenish this loss and preferentially excite frequencies close to a global eigenfrequency. Such stochastic excitation can maintain a narrow spectral peak; it does not by itself guarantee the exceptionally stable long-term phase required for pulsar timing. A physical account of coherence must also address how phase fluctuations are suppressed or limited.

The working proposition of this chapter is therefore modest but concrete: the size and field structure of a neutron-star magnetosphere permit electromagnetic travel times and geometric LC estimates in the millisecond-to-tens-of-milliseconds regime. Establishing a specific stable resonance requires a coupled electrodynamic/plasma eigenmode calculation. In the following chapters, the global mode will be used as a hypothesis for the recurrent velocity pattern of magnetospheric emitting regions, rather than treated as a previously demonstrated property of neutron stars. **[3]**

4. Excitation and Stability of Magnetospheric Oscillations

The characteristic frequency of a resonator does not, by itself, explain why its oscillations persist. The proposed magnetospheric mechanism therefore distinguishes three processes: irregular injection of electromagnetic energy, selective excitation of a global resonant mode, and a mechanical or magnetohydrodynamic response of surrounding plasma. The global mode may provide a recurring temporal structure while local disturbances alter the instantaneous geometry of the emitting regions.

This chapter develops an energy-consistent equivalent model for these processes. It does not assume that randomly timed disturbances automatically produce the long-term phase stability of observed pulsars. Instead, it identifies the quantitative conditions that a magnetospheric resonance would have to satisfy.

4.1. Random Electromagnetic Excitation from the Neutron Star

Electric currents, evolving plasma structures and magnetic disturbances near the neutron-star surface can inject electromagnetic energy into the magnetosphere. Rather than requiring a periodic driver, the model allows many irregular disturbances whose temporal spectrum includes frequencies near the characteristic global resonance.

Let q(t) denote the equivalent charge coordinate of one global electromagnetic mode. Its simplest driven equation is

$$L\,d^2q/dt^2 + R\,dq/dt + \frac{q}{C} = V_e(t).$$

Here L and C represent effective modal inductance and capacitance, R is a dissipative parameter, and Vext(t) is a generalized electromotive drive. The last quantity is not necessarily a voltage between two literal metal electrodes; it describes how electromagnetic disturbances couple to the mode.

The associated undamped frequency is

$$\omega_0 = \frac{1}{\sqrt{(LC)}}, \quad f_0 = \frac{\omega_0}{2\pi}.$$

Broadband forcing can generate a strong response around f_o even if the driving events have no preferred repetition period. This is resonant filtering of an irregular input, not a claim that the stellar disturbances themselves occur at f_o.

4.2. Excitation by the Surrounding Environment

The magnetosphere is also affected by disturbances originating outside the star, including changes in the surrounding plasma and externally propagating electromagnetic perturbations. The effectiveness of any disturbance is determined by its coupling to the relevant eigenmode; a large energy release need not excite that mode efficiently.

We may write the total effective drive as the sum of stellar and environmental contributions:

$$V_e(t) = V_s(t) + V_a(t).$$

In statistical terms, the power spectrum of the response is the input power spectrum weighted by the squared frequency response of the resonator:

$$S_q(\omega) = |H(\omega)|^2\, S_V(\omega),$$

with

$$H(\omega) = \frac{1}{1/C - L\omega^2 + iR\omega}.$$

This formula applies to a stationary linear system with a well-defined input spectrum. If the two driving sources are correlated, their cross-spectral terms must also be included in S_V. A sharp response peak demonstrates frequency selection, but does not by itself establish coherence over many years.

4.3. Local Magnetohydrodynamic Oscillations and Turbulence

A global electromagnetic mode need not imply a uniform or mechanically rigid motion of the magnetosphere. Local plasma structures may support Alfvénic and compressional motions, with different natural frequencies, damping rates and spatial phases. Turbulent activity may coexist with these organized oscillations.

For one local mechanical coordinate $x_i(t)$, a useful linear approximation is

$$m_i\,d^2x_i/dt^2 + 2m_i\gamma_i\,dx_i/dt + k_ix_i = g_iq + F_i(t).$$

The effective inertia m_i and restoring coefficient k_i describe a particular plasma deformation, γ_i its damping, g_i the coupling to the global electromagnetic coordinate, and $F_i(t)$ local irregular forcing. The corresponding uncoupled natural frequency satisfies $\omega_i^2 = k_i/m_i$.

A driven local mode can respond at the global frequency even when ω_i differs from ω_o.

However, its response amplitude and phase lag depend on the frequency difference and damping. Other self-excited or transient disturbances may remain superimposed; the global mode need not suppress all turbulence.

4.4. Coupling Between Local Oscillations and Global Resonance

The interaction must be bidirectional: magnetospheric deformation can alter the current distribution and electric-field energy, while electromagnetic forces act back on the plasma. To preserve the energy accounting, the simplest coupled model uses a shared interaction energy proportional to the product qx_i.

$$L\ddot{q} + R\dot{q} + \frac{q}{C} - \Sigma g_i x_i = V_e(t),$$

$$m_i\ddot{x}_i + 2m_i\gamma_i\dot{x}_i + k_i x_i - g_i q = F_i(t).$$

For this equivalent model the stored energy is

$$W = \frac{1}{2}L\dot{q}^2 + \frac{q^2}{2C} + \Sigma[\frac{1}{2}m_i\dot{x}_i^2 + \frac{1}{2}k_i x_i^2 - g_i q x_i].$$

Differentiating W and using the equations of motion gives

$$dW/dt = V_e\dot{q} + \Sigma F_i\dot{x}_i - R\dot{q}^2 - \Sigma 2m_i\gamma_i\dot{x}_i^2.$$

Thus the source terms supply power, while resistive and mechanical damping remove it. Internal coupling exchanges energy but cannot create energy. This consistency is essential when irregular events are proposed as the energy source of a sustained resonance.

The coefficients g_i, k_i and m_i are not measured in the present model. They would have to be calculated from the field geometry, plasma properties and boundary conditions. The equations therefore establish a testable coupling framework rather than a completed magnetospheric eigenmode solution.

4.5. Resonance Stability, Damping, and Phase Fluctuations

For a weakly damped mode with characteristic angular frequency ω_o, modal energy W and quality factor Q, the mean dissipated power is approximately

$$P_l \approx \frac{\omega_0 W}{Q}.$$

Maintained oscillations require the mean power coupled into the global mode to balance both its direct losses and any net power transferred to dissipative local motions. A useful illustrative case is f_o = 50 Hz, W = 10^{20} J and Q = 10^4, giving

$$P_l \approx 3.14 \times 10^{18}\ \mathrm{W}.$$

The energy lost per 20 ms cycle in the same weak-damping approximation is approximately 6.28 × 10^{16} J. Both the modal energy and quality factor in this illustration are freely chosen; they are not inferred from neutron-star observations. A larger Q reduces the power required to maintain a fixed energy but does not, by itself, establish a source of energy.

Illustrative quality factor Q	Amplitude e-folding time at 50 Hz	Loss fraction per cycle
10^2	0.637 s	≈ 6.28 %
10^3	6.37 s	≈ 0.628 %
10^4	63.7 s	≈ 0.0628 %
10^5	637 s	≈ 0.00628 %

Table 1. Passive resonator approximations; fractional losses use the weak-damping expression $2\pi/Q$.

A second distinction is crucial. Random impulses can act in either direction in phase space. For unbiased, independent small phase increments $\Delta\phi_j$, the mean accumulated phase shift may vanish, while its statistical dispersion grows:

$$E(\Delta\Phi_N) = 0, \quad Var(\Delta\Phi_N) = N\,Var(\delta\varphi).$$

If excitation events occur at mean rate λ, the simplest phase-diffusion approximation is

$$\sigma(\Phi, t) \approx \sigma(\varphi)\sqrt{(\lambda t)}.$$

This result is conditional on independent increments of fixed variance; correlated events, feedback or amplitude-dependent dynamics can change it substantially. The frequency selectivity of a passive resonator does not eliminate phase diffusion. Consequently, it is not sufficient to infer the precision of pulsar timing directly from the LC resonance or from the zero mean of random phase kicks.

An intrinsically maintained nonlinear oscillation might reduce amplitude variations and phase sensitivity, but it requires a physically specified feedback mechanism. Alternatively, extremely weak coupling of stochastic disturbances to the phase coordinate could allow a relatively stable clock. Neither mechanism is yet derived for the proposed magnetosphere.

Observational timing studies find that the average pulse profile can remain stable despite strong variations in individual pulses, while timing noise and sudden timing events occur in many pulsars. These observations provide quantitative constraints that any resonance-driven explanation must reproduce [7, 8, 10].

In summary, irregular electromagnetic activity offers a possible supply of energy to a global resonant mode, and electromagnetic coupling offers a possible route by which local plasma motion follows its preferred frequency. The existence of a stable, long-lived phase and its connection to the observed pulse profile remain independent physical requirements. They will be treated as predictions to be tested, not assumed consequences of random excitation. **[7], [8]**

5. Three-Dimensional Oscillations of the Magnetosphere

The global electromagnetic resonance introduced in Chapter 3 specifies a characteristic time scale, but not the three-dimensional geometry of the resulting magnetospheric motion. The latter is essential in the proposed model because the arrival-time structure of radiation depends on the spatial and temporal distribution of velocities in the emitting plasma. This chapter develops a simple axisymmetric deformation, identifies the relevant magnetic restoring forces, and estimates the corresponding velocity scales. The model is deliberately kinematic at first: neither a particular field-line eigenfunction nor a measured magnetospheric displacement amplitude is assumed.

5.1. Equatorial Expansion and Polar Contraction

Consider a magnetosphere whose reference outer boundary is approximated by a sphere of radius R_o. Its lowest-order axisymmetric quadrupolar deformation can be represented by alternating equatorial expansion and polar contraction. A convenient one-parameter boundary model is

$$R_{eq}(t) = R_0\,[1 + q(t)], \qquad R_{pol}(t) = \frac{R_0}{[1 + q(t)]^2}.$$

The product $R_e q^2 R_pol$ is then constant: the ellipsoidal boundary has the same enclosed volume as the reference sphere. For a single harmonic motion, let

$$q(t) = q_0 \cos(\omega t), \qquad \omega = 2\pi f.$$

For a deformation with $|q|$ much smaller than unity, the equatorial displacement is $R_o q$ and the polar displacement is approximately minus twice that value. Thus the two directions respond with opposite signs but at the same frequency. Volume conservation is a useful geometrical constraint rather than a necessary property of a real magnetosphere; compression, field-aligned flow, and changes in particle density may also occur.

A spherical reference boundary is not claimed to be the exact equilibrium shape of a dipolar pulsar magnetosphere. Rotation, plasma

currents, magnetic topology, external pressure and open field lines can produce a strongly nonspherical configuration. The spherical-to-ellipsoidal construction serves to specify a reproducible test deformation.

5.2. Magnetic Pressure and Restoring Forces

In magnetized plasma, the Lorentz force density can be written as a sum of magnetic-pressure and magnetic-tension terms:

$$f_{mag} = \frac{(\nabla \times B) \times B}{\mu_0} = -\nabla \frac{B^2}{2\mu_0} + \frac{(B \cdot \nabla)B}{\mu_0}.$$

Magnetic pressure opposes appropriate changes in field strength, while magnetic tension opposes the bending of field lines. Either contribution may participate in the restoring force, depending on the equilibrium and on the displacement pattern. A strong background field does not alone establish a stable oscillation: the magnetic energy of the perturbed configuration must have positive curvature about the actual equilibrium after all appropriate field, plasma and boundary terms are included.

Let ξ(r,t) denote the Lagrangian displacement of the plasma. In ideal magnetohydrodynamics, the first-order magnetic perturbation is

$$\delta B = \nabla \times (\xi \times B_0).$$

The net restoring tendency may be expressed through a quadratic modal energy and an effective inertia,

$$\delta W = \frac{1}{2} K_2 q^2, \quad \omega_2^2 = \frac{K_2}{M_2}.$$

Here K_2 is the stiffness associated with the chosen deformation q, and M_2 is its generalized inertia. Positive K_2 is required for stability of this particular mode; establishing the stability of the full magnetosphere requires a more general eigenmode or energy-principle analysis. The previous homogeneous-field and prescribed-deformation exercises should therefore not be treated as independent determinations of the quadrupolar eigenfrequency.

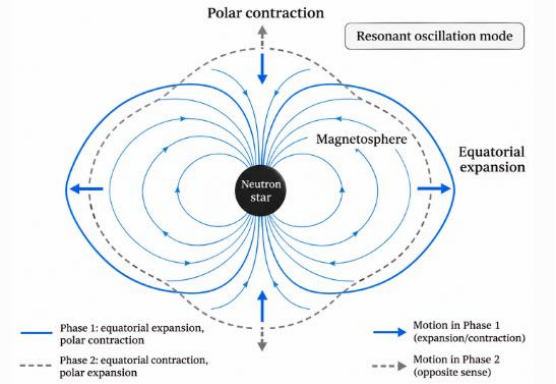


Figure 1. *Schematic illustration of the resonant oscillation mode of the neutron-star magnetosphere, showing alternating equatorial expansion and polar contraction. The dashed contour represents the opposite phase of the oscillation.*

5.3. Spatial Distribution of Oscillation Velocities

A deformation that moves the stellar surface together with the entire magnetosphere is not appropriate, because magnetospheric field lines are anchored in the star. We therefore introduce a radial envelope h(r) that vanishes at the stellar surface and increases toward an outer reference radius R_m. A simple smooth choice is

$$s = \frac{r - R_*}{R_m - R_*}, \quad h(r) = 3s^2 - 2s^3, \quad 0 \le s \le 1.$$

For a schematic Cartesian quadrupolar displacement, with the z-axis aligned with the magnetic axis, write

$$\xi(r,t) = q(t)h(r)\,[x\,e_x + y\,e_y - 2z\,e_z].$$

This trial displacement vanishes at the stellar surface and produces the desired opposite transverse and axial motions near the outer boundary. Because h varies with radius, the trial field is not exactly divergence-free

throughout the interior, even though its outer-boundary deformation is volume-preserving at leading order. A fully incompressible mode would require an additional transverse correction determined by the continuity equation.

The local plasma velocity then follows by differentiation:

$$u(r,t) = \frac{\partial \xi(r,t)}{\partial t} = q_0 \omega\, h(r) \sin(\omega t)\,[-x\, e_x - y\, e_y + 2z\, e_z].$$

The minus sign reflects the derivative of cos(ωt). Different points possess different velocities even though the entire displacement shares one basic frequency. This is precisely the property required for testing arrival-time differences from spatially separated emission regions. The velocity relevant to an observer in direction n is the projection u_r = n · u; only that projection enters the proposed propagation law c + u_r discussed in Chapter 2.

The trial pattern is not a solved normal mode of a dipolar, current-carrying magnetosphere. In particular, its phase and radial envelope must eventually be obtained from the coupled electromagnetic and plasma boundary-value problem, not chosen solely to obtain a desired pulse profile.

5.4. Small-Amplitude Oscillations

For a sinusoidal displacement of amplitude A at a given location, the maximum local speed and acceleration are

$$u_{max} = \omega A, \qquad a_{max} = \omega^2 A.$$

The linear resonance frequency is independent of the displacement amplitude within the validity range of linear theory. Consequently, a macroscopic field structure can oscillate at a well-defined frequency while the motion of an individual plasma element is minute. The equivalent LC mode also does not require every part of the plasma to move with the same amplitude.

Local displacement amplitude	Maximum speed at 50 Hz	Maximum acceleration at 50 Hz
1 m	314 m/s	9.87×10^4 m/s²
1 mm	0.314 m/s	98.7 m/s²
10 nm	3.14 µm/s	9.87×10^{-4} m/s²

***Table 1**. Harmonic velocity and acceleration scales for one local displacement component. These are illustrative amplitudes, not measured pulsar parameters.*

For a field structure with reference radius 1000 km, a global boundary deformation with an equatorial amplitude of 1 m corresponds to $q_o = 10^{-6}$; the corresponding polar boundary amplitude is approximately 2 m. For the amplitude 10 nm, the same ratios are smaller by eight orders of magnitude. The stiffness, stored oscillatory energy and radiative coupling must nevertheless be specified before any of these amplitudes can be selected on physical grounds.

In the proposed c + u_r propagation model, very small differences in radial velocity may significantly affect calculated travel-time differences across astronomical distances. That statement does not establish either the proposed propagation law or a pulse-brightening mechanism. In particular, simultaneous arrival of radiation emitted at one instant is not the same as compression of successive emission times. Chapter 6 will retain that distinction explicitly.

5.5. Influence of Slow Stellar Rotation

The fundamental version of the resonant-emission model does not require the neutron star to rotate. Nevertheless, slow rotation can be included as a perturbation of the plasma dynamics. In a frame rotating with the star, the Coriolis acceleration is

$$a_{Cor} = -2\Omega \times u,$$

where Ω is the stellar angular-velocity vector. The largest ratio of Coriolis acceleration to the restoring acceleration of a sinusoidal local displacement is approximately

$$\frac{a_{Cor,max}}{a_{osc,max}} \leq \frac{2\Omega}{\omega} = \frac{2T_{osc}}{T_{rot}}.$$

For a resonant period T_osc = 20 ms, the results are:

Stellar rotation period	Angular velocity Ω	Upper bound 2Ω/ω
1 hour	1.745×10^{-3} rad/s	1.11×10^{-5}
3 hours	5.818×10^{-4} rad/s	3.70×10^{-6}
6 hours	2.909×10^{-4} rad/s	1.85×10^{-6}

***Table 2**. Relative magnitude of the Coriolis term for slow stellar rotation and a 50 Hz local oscillation.*

For these illustrative rotation periods, the direct Coriolis perturbation is small compared with the acceleration of the selected fast mode. Rotation can nonetheless modify the geometry of a narrowly directed signal over many oscillation cycles and may weakly couple otherwise distinct transverse and axial motions. Neither an effective two-pulse profile nor a particular polarization pattern follows from the Coriolis term alone. Such predictions require a spatial radiation calculation and an eigenmode solution.

The discussion therefore adopts nonrotating or slowly rotating stars as the simplest setting for the resonant-emission hypothesis, without asserting that actual pulsars are nonrotating. The conventional rotating-magnetosphere interpretation and the observational evidence supporting it remain the reference against which any alternative calculation must be compared. **[3]**

6. Spatial and Temporal Concentration of Radiation

The previous chapters introduced a global electromagnetic resonance and a spatially distributed oscillatory velocity field in the magnetosphere. This chapter specifies the second part of the proposed emission mechanism: how radiation emitted by different magnetospheric locations is mapped into the arrival times measured by a distant observer. The distinction between spatial coincidence of arrivals and compression of successive emission times is essential. The analysis is conditional on the source-dependent propagation law introduced in Part C2, and does not represent a consequence of conventional vacuum electrodynamics. [18]

6.1. Radiation Emitted Toward a Distant Observer

Let S be an active radiating region of the magnetosphere. Each infinitesimal surface element dS is assumed to emit energy into a range of directions, including the observer's line of sight. The observer therefore does not require magnetospheric reflection or conventional optical refraction in order to receive radiation from every participating surface element. The quantity that remains to be calculated is the temporal distribution of the received energy.

Let r(s,t_e) denote the location of a source element, R_o the fixed position of an observer, and n the unit vector directed approximately from the star toward the observer. The source-to-observer distance and the source velocity projected toward the observer are

$$L_s(t_e) = |R_o - r(s,t_e)|, \qquad u_s = n \cdot \frac{\partial r}{\partial t_e}.$$

For a distant observer and a compact magnetosphere, L_s is approximately D − n·r, where D is the distance from a reference point near the star. Radiation strength per surface area and per unit solid angle is denoted by j(s,t_e,n). This emissivity may depend on direction, frequency and polarization. The simplest numerical examples will take it constant and isotropic; this assumption should not be

mistaken for a measured property of a pulsar magnetosphere.

6.2. Propagation Time from Different Magnetospheric Regions

As a test hypothesis, let the propagation velocity along the observer direction depend on the radial velocity of the emitting element at the instant of emission. Using a positive u_s for motion toward the observer, the proposed rule is

$$v_{prop} = c + u_s.$$

Assuming the emitted signal subsequently travels at this assigned speed along its path, the observer receives a signal emitted at time t_e at

$$t_p\,(s, t_e) = t_e + \frac{L_s}{c + u_s}.$$

This expression is the central arrival-time hypothesis of the study. In established vacuum electrodynamics the propagation speed is c irrespective of source velocity; thus the source-dependent term must be evaluated experimentally rather than inferred from the existence of pulsed radiation. The sign convention and the motion of the source position must be applied consistently: an approaching source has positive u_s and a decreasing L_s.

For speeds much smaller than c, the arrival-time map can be expanded to first order as

$$t_p \approx t_e + \frac{D}{c} - \frac{n \cdot r}{c} - \frac{D\,u_s}{c^2}.$$

The two correction terms have distinct origins. The first is the geometric change of path length; the second is the assumed velocity dependence of propagation. A common delay D/c has no effect on the measured pulse shape.

6.3. Spatial Synchronization of Arrival Times

Consider many surface elements radiating at one common emission time t_o. Their arrival times are synchronized when

$$t_p\,(s, t_0) \approx constant \quad for\ s \in S_a,$$

where S_a is the active subset of the magnetosphere. For two elements with nearly equal propagation speeds, the first-order condition becomes

$$\Delta u \approx \frac{c\,\Delta L}{D}.$$

For example, at D = 6200 light-years, compensating a 450 km difference in source depth requires a difference in radial speed of approximately 2.30 μm/s. If the emitting points lie in a transverse plane, their geometric path differences are vastly smaller. The relevant velocity distribution therefore depends on the observer direction and the three-dimensional source geometry.

A single spatial synchronization event does not, by itself, create a brightness pulse from a continuously emitting source. Constant emitters contribute energy to the observer at all times even if their absolute propagation delays differ. Their delay functions must change over time, or the emitted power and directional emissivity must change, to obtain temporal modulation. Spatial coincidence can alter the timing of a finite, intrinsically synchronized event; temporal compression of continuing emission requires the additional condition developed next.

6.4. Temporal Compression of Continuous Radiation

For a single source element, define the arrival-time Jacobian $J_s = \partial t_p / \partial t_e$.

Differentiating the full propagation-time law gives

$$J_s = \frac{\partial t_p}{\partial t_e} = 1 + \frac{\partial L_s / \partial t_e}{c + u_s} - \frac{L_s\, a_s}{c + u_s{}^2},$$

where $a_s = \partial u_s / \partial t_e$ is the projected acceleration of the emitting element. Because its line-of-sight distance decreases as it approaches the observer, $\partial L_s / \partial t_e \approx -u_s$. The first-order form for small velocities is therefore

$$J_s \approx 1 - \frac{u_s}{c} - \frac{D a_s}{c^2}.$$

The velocity term is negligible for the nanometer-amplitude, high-frequency examples considered below; the acceleration term can become significant because it is multiplied by the large observer distance D. Strong temporal compression occurs when the positive Jacobian is much smaller than unity. At $J_s = 0$ the idealized mapping develops a caustic; the divergence of a point-source approximation cannot be used as a physical prediction of infinite intensity.

The condition for appreciable compression is therefore controlled primarily by acceleration and source distance, not simply by the equality of propagation delays among neighboring surface elements. For an approximately fixed $L_s = D$the characteristic acceleration scale is

$$a_{crit} \approx \frac{c^2}{D}.$$

For D = 6200 light-years, this scale is approximately 1.53 × 10^{-3} m/s². This is a derived mathematical scale in the proposed c + u model, not an observed acceleration of pulsar plasma.

6.5. Conditions for the Formation of Bright Pulses

Conservation of emitted energy gives a simple transport equation for the observed energy flux. Let $j(s, t_e, n)$ be the power per source area per unit emitted solid angle, and neglect absorption along a path of length L_s. The contribution of an emitted interval dt_e to an observed interval dt_p is

$$dE = j(s, t_e, n)\, dS\, d\Omega\, dt_e.$$

Hence, in the geometric-optics and incoherent-intensity approximation, the received energy flux per unit observer area is

$$F(t_p, n) = \int_S \sum_{roots} \frac{j(s, t_e, n)}{L_s^2\, |J_s|}\, dS.$$

The sum extends over all emission times that map to the given arrival time. For monotonic maps there is one root per surface element; a nonmonotonic map may have several. In either case, energy transported over a complete mapping interval must be counted once per emitted element and cannot be created by focusing. Finite emission bandwidth, source size, coherence and transport physics regularize idealized mathematical caustics.

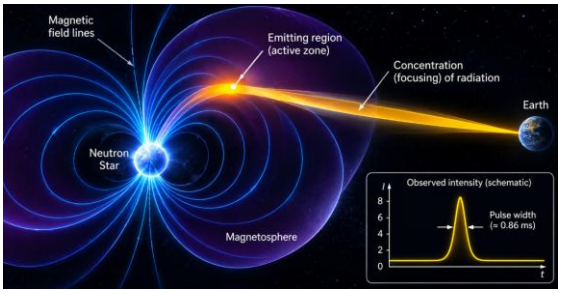


Figure 2. Spatial and temporal concentration of magnetospheric radiation at a distant observer. *An active region of the neutron-star magnetosphere emits electromagnetic radiation toward Earth. In the proposed source-dependent propagation model, the spatial and*

temporal distribution of source velocities modifies the arrival times of radiation emitted from different locations and at successive instants. Under suitable conditions, these contributions become concentrated within a short observation interval, producing a bright pulse. The inset illustrates the resulting intensity enhancement. The diagram is schematic and not to scale.

For steady equal emitters, their unmodulated fluxes add. An enlarged active surface therefore increases the total contribution proportionally only if the emissivity per unit area and the relevant directional throughput remain unchanged. A bright periodic pulse requires, in addition, time-dependent transport Jacobians, intrinsic emissivity modulation or time-dependent directional radiation. The area controls the amount of participating energy, while the temporal map controls its distribution over the observed pulse.

6.6. Dependence of Pulse Intensity on the Active Emitting Area

To separate these effects, consider N equal subregions with the same mean emissivity j_0 and a common distance D. Their observed flux is schematically

$$F(t) = \frac{j_0 A}{D^2} G(t), \qquad G(t) = \langle 1/|J| \rangle.$$

where A is the total active area and the angular brackets represent the average of the relevant arrival-time factors across that area. If J is unchanged, scaling A by a factor of ten scales both the instantaneous flux and the mean flux by ten, without changing the pulse-to-mean contrast. Conversely, changing J can vary the contrast even at constant A. A single contiguous emitting region is sufficient for the model; a collection of small patches need not be introduced unless observations demand it.

As an explicit one-region example, take a sinusoidal radial velocity and define the dimensionless compression strength κ by

$$u(t_e) = \frac{\kappa\, c^2}{D\omega} \sin(\omega t_e), \qquad 0 < \kappa < 1.$$

After subtracting the common travel time and neglecting the much smaller source-position term, the arrival-time map and its derivative are

$$\tau = t_e - \frac{\kappa}{\omega} \sin(\omega t_e), \qquad J = 1 - \kappa \cos(\omega t_e).$$

For constant emitted power into the observed direction, the intensity enhancement relative to the cycle-averaged flux is

$$\frac{F(\tau)}{F_{avg}} = \frac{1}{1 - \kappa \cos\left(\omega t_e(\tau)\right)}.$$

For the Crab-like working period T = 33.5 ms, choose κ = 0.90. The peak enhancement is 10.0, the minimum is 0.526, and the maximum-to-minimum ratio is 19.0. The full width at half of the peak-to-minimum contrast is approximately 0.63 ms. The average of the observed intensity over one received cycle remains exactly the baseline level; the short bright phase is balanced by a longer dimmer phase.

Compression strength κ	Peak / mean	Minimum / mean	Peak / minimum
0.50	2.00	0.667	3.0
0.80	5.00	0.556	9.0

Compression strength κ	Peak / mean	Minimum / mean	Peak / minimum
0.90	10.00	0.526	19.0
0.98	50.00	0.505	99.0

***Table 1**. Predicted flux contrast for the idealized monotonic sinusoidal arrival-time map at constant emitted power.*

The example does not determine the actual radio or gamma-ray luminosity of the Crab pulsar. Its numerical amplitudes are chosen to illustrate how the hypothesized kinematic map can change a continuous emission profile. A physically complete estimate must also determine the emissivity and angular distribution of radiation, and must compare the predicted spectrum and polarization with measured data.

6.7. Dependence of the Observed Pulse Profile on Viewing Direction

Let the dominant oscillatory velocity lie along a fixed axis, while the observer views that axis at angle θ. The relevant projected speed is $u_r = u.cos\theta$. Under the same simplifications, the projected compression strength becomes κ cos θ and the Jacobian is

$$J(\theta, t_e) \approx 1 - \kappa \cos\theta \cos(\omega t_e).$$

At θ = 0° the contrast is strongest; at θ = 90° the velocity projection vanishes and this mechanism produces no temporal modulation. A viewing direction on the opposite side of the oscillation axis reverses the phase at which the maximum is received. The same magnetosphere can therefore appear strongly pulsed, weakly pulsed or almost constant to observers located in different directions.

Viewing angle θ	Peak / mean	Minimum / mean	Peak / minimum
0°	10.00	0.526	19.00
30°	4.54	0.562	8.07
60°	1.82	0.690	2.64
90°	1.00	1.000	1.00

***Table 2**. Direction-dependent pulse contrast for κ = 0.90. Angles refer to the assumed velocity-oscillation axis.*

The model consequently predicts a viewing-angle selection effect: observing a periodic stellar magnetosphere need not imply the presence of detectable pulsations along every line of sight. Intrinsic anisotropy, distinct northern and southern source regions, and frequency-dependent propagation could add further structure, including multiple pulse maxima, but those extensions are treated separately in the following chapters.

The quantitative results in this chapter are conditional on the hypothesis that the assigned propagation speed c + u_s persists after emission. The standard vacuum value c does not yield the distance-amplified compression used here. An independent measurement of the source-velocity dependence of propagation is therefore a direct falsifiability test, not a subsidiary detail of the proposed pulsar mechanism.

7. Quantitative Model of Pulsar Emission

The preceding chapters proposed that a global electromagnetic oscillation can impose a common frequency on spatially distributed regions of a neutron-star magnetosphere. This chapter constructs an explicit, reproducible model of the resulting signal received by a distant observer. Its purpose is to distinguish a

calculated pulse profile from a schematic description of pulse formation. The model is deliberately minimal: five continuously emitting regions undergo sinusoidal motion, while the observer's viewing direction is varied.

The calculation is conditional on the source-dependent propagation law introduced in Section 2 and examined separately in Part C2. In particular, the assumption that radiation retains a propagation speed of $c + u$ after emission is **not** part of established vacuum electrodynamics. Agreement between the computed profile and a measured pulse would not, by itself, establish this propagation law.

7.1. Five-Region Magnetospheric Model

The active region is represented by five equally weighted emitting elements located along a transverse coordinate x. Their reference positions are

$$x_i = (-225,\ -112.5,\ 0,\ 112.5,\ 225)\ \text{km}.$$

Its total extent is thus 450 km. Every element is assumed to emit continuously, isotropically in the simplified source description, and with the same time-independent spectral power within the selected observational band. This is a model of a participating region, not a measurement of an actual Crab-pulsar emitting area. The spatial extension is treated as sufficiently small in comparison with the observer distance that a far-field expansion applies.

For a numerical example, choose a period comparable to that of the Crab pulsar, a source distance of 6200 light-years, and a common angular frequency:

$$T_0 = 33.5\ \text{ms}, \qquad f_0 = \frac{1}{T_0} = 29.8507\ \text{Hz}, \qquad \omega_0 = \frac{2\pi}{T_0} = 187.558\ \text{rad s}^{-1}.$$

$$D = 6200\ \text{ly} \simeq 5.866 \times 10^{19}\ \text{m}.$$

The distance and period are rounded illustrative inputs. No claim is made that the current magnetospheric extent or local velocities have been measured independently.

7.2. Sinusoidal Velocity Distribution

Let the common oscillation axis be the z axis. Each emitting element has a velocity component along that axis,

$$u_i(t_e) = U_i \sin(\omega_0 t_e),$$

where t_e denotes emission time. The amplitudes are parameterized as

$$U_i = \kappa_i \frac{c^2}{D\omega_0}, \qquad (\kappa_1, \ldots, \kappa_5) = (0.85,\ 0.88,\ 0.90,\ 0.88,\ 0.85).$$

The κ_i are dimensionless model parameters. They have been chosen to demonstrate pronounced but nonsingular temporal concentration; they are **not derived from** the global LC dynamics. A sinusoidal displacement associated with each velocity is $z_i(t_e) = -(U_i/\omega_0)\cos(\omega_0 t_e)$, up to a constant offset. The corresponding velocity and displacement amplitudes are listed in Table 1.

El.	Position x_i (km)	κ_i	Velocity amplitude U_i (μm/s)	Displacement amplitude (nm)
1	-225.0	0.85	6.944	37.02
2	-112.5	0.88	7.189	38.33
3	0.0	0.90	7.352	39.20

El.	Position x_i (km)	κ_i	Velocity amplitude U_i (μm/s)	Displacement amplitude (nm)
4	112.5	0.88	7.189	38.33
5	225.0	0.85	6.944	37.02

Table 1. *Prescribed velocity amplitudes in the five-element model. The nanometre-scale displacements follow from the adopted 33.5-ms period and the postulated propagation relation.*

These small amplitudes are compatible with a linear-oscillation *kinematic ansatz*. Their ability to develop spontaneously as a coupled magnetospheric mode remains a separate dynamical question.

7.3. Arrival-Time Mapping

Consider an observer at an angle θ to the z axis. To leading order, the line-of-sight velocity of element i is

$$u_{r,i}(t_e,\theta) = U_i \cos\theta \sin(\omega_0 t_e).$$

With the proposed propagation speed $c + u_{r,i}$, the arrival time is

$$t_{p,i} = t_e + \frac{L_i(t_e,\theta)}{c + u_{r,i}(t_e,\theta)}.$$

For $D \gg |x_i|$ and $|u_{r,i}| \ll c$, the line-of-sight path can be expanded as $L_i \simeq D - x_i \sin\theta$, apart from the negligible effect of the assumed nanometre displacement. Subtracting the common propagation time D/c gives the reduced arrival time $\tau_i = t_{p,i} - D/c$:

$$\boxed{\tau_i(t_e,\theta) \simeq t_e - \frac{x_i \sin\theta}{c} - \frac{\kappa_i \cos\theta}{\omega_0} \sin(\omega_0 t_e).}$$

Differentiating with respect to emission time yields

$$\boxed{J_i(t_e,\theta) = \frac{\partial \tau_i}{\partial t_e} \simeq 1 - \kappa_i \cos\theta \cos(\omega_0 t_e).}$$

The factor J_i is the local Jacobian of the time mapping. A value below unity means that a finite interval of emission time is received in a shorter interval; a value above unity means temporal spreading. In the chosen example $\kappa_i \leq 0.9$, so $J_i \geq 0.1$ for all viewing directions between $0°$ and $90°$. The map is therefore monotonic, and there is exactly one emission time contributing to each arrival time for each element.

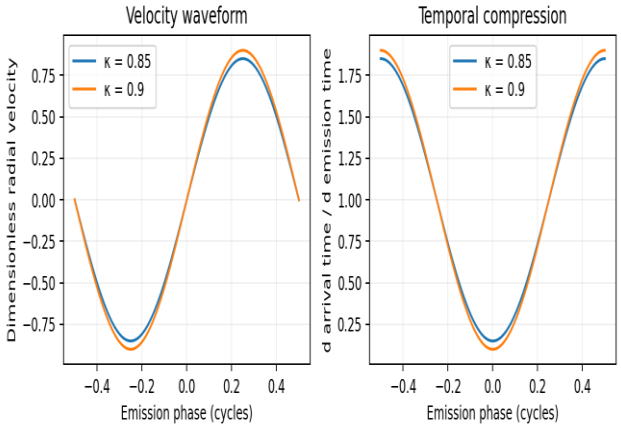


Figure 3. Example dimensionless velocity curves and arrival-time Jacobians for two values of the concentration parameter. Strong compression occurs near a minimum of J_i, without introducing a mathematical caustic in this example.

7.4. Calculation of the Observed Light Curve

Let $F_{i,0}$ be the mean received flux that would be contributed by element i at the same distance in the absence of temporal remapping. Under the simplified energy-accounting assumption that a finite emitted energy packet is assigned to its corresponding interval of arrival time, conservation of packet energy gives

$$F_i(\tau_i)\, d\tau_i = F_{i,0}\, dt_e.$$

Hence the instantaneous received flux from element i is

$$F_i(\tau) = \frac{F_{i,0}}{\left|J_i\left(t_{e,i}, \theta\right)\right|},$$

where the relevant emission time $t_{e,i}$ must be found from the arrival-time equation at the specified observer time τ. The total signal is the sum over all five regions. For equal intrinsic contributions and a normalization $\overline{F} = \sum_i F_{i,0}$, this becomes

$$\boxed{\frac{F(\tau,\theta)}{\overline{F}} = \frac{1}{5}\sum_{i=1}^{5} \frac{1}{1 - \kappa_i \cos\theta \cos\left(\omega_0 t_{e,i}\right)}.}$$

The inverse equations are solved numerically for every observer time using a monotone Newton iteration. Importantly, $t_{e,i}$ is generally **not** equal to τ; inserting the observer time directly into the cosine would give an incorrect pulse profile when temporal compression is appreciable.

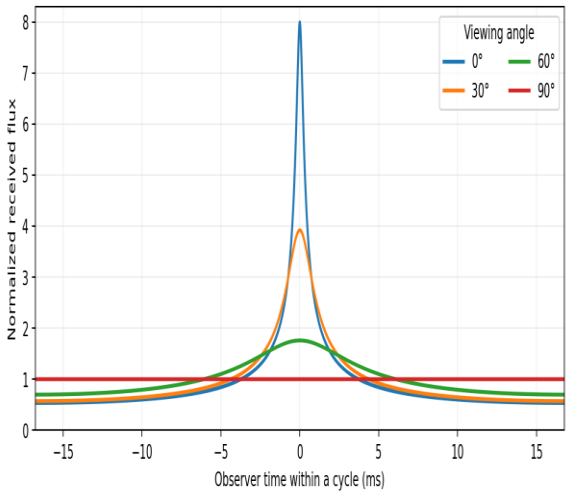


***Figure 4**. Numerically calculated received light curves for four viewing directions. Each curve is normalized by its own full-cycle mean, which equals unity for this non-caustic conservative mapping. The same oscillating emitter appears strongly pulsed, weakly pulsed, or unmodulated depending on the viewing angle.*

7.5. Pulse Width, Intensity, and Temporal Compression

The computed profiles have been sampled densely over one period. The peak and minimum intensities are expressed in units of the period-averaged received flux. A pulse width $W_{1/2}$ is defined here as the full width at **half the difference between the minimum and maximum**, rather than the width at half the peak above zero. This explicit convention avoids ambiguity when the minimum intensity is nonzero.

Viewing angle θ	Peak $F/\overline{F}$	Minimum $F/\overline{F}$	Peak/minimum	$W_{1/2}$ (ms)
0°	8.000	0.534	14.97	0.86
30°	3.920	0.570	6.88	2.54
60°	1.759	0.697	2.52	7.89
90°	1.000	1.000	1.00	No pulse

***Table 7.2**. Quantitative viewing-angle dependence of the five-region model. The values are derived from the prescribed velocity profiles rather than independently fitted to a specific observed pulse.*

For an observer on the oscillation axis, the minimum Jacobian of the central element is $J_{3,\min} = 1 - 0.90 = 0.10$. This element alone can therefore attain an instantaneous flux enhancement of ten relative to its own mean. Combining all five elements with slightly different parameters produces a total normalized peak of 8.0. The integrated energy over one complete arrival-time period is unchanged:

$$\int_{\tau_0}^{\tau_0+T_0} F_i\left(\tau\right) d\tau = F_{i,0} T_0.$$

Thus the mechanism redistributes received energy in time in the assumed model; it does not create energy. The high peak is

compensated by intervals of lower intensity.

7.6. Comparison of Different Observer Directions

At $\theta = 0°$, the line of sight is aligned with the imposed oscillation axis, and temporal compression is strongest. At $30°$ and $60°$, only the velocity component projected along the line of sight contributes. The pulses become progressively wider and weaker. At $90°$, the oscillation has no line-of-sight velocity component, $J_i = 1$, and the received flux is constant within the assumptions of uniform emission.

For oblique viewing, the transverse extent of the region introduces different *constant* propagation delays $-x_i \sin\theta / c$. These shifts can change the relative alignment of contributions, although they do not by themselves alter the mean flux of continuously emitting regions. A different observer thus need not detect the same pulse profile, even when the underlying LC frequency and intrinsic emissivity are identical.

This angular dependence is a falsifiable feature of the proposed propagation-and-oscillation model. The numerical comparison alone does not establish that real magnetospheres produce the required aligned sinusoidal velocities. Moreover, the calculation predicts a direction-dependent temporal profile, **not** optical beam steering: radiation from all five elements is assumed to be emitted toward all viewing directions from the outset.

7.7. Continuous, Weakly Pulsating, and Strongly Pulsating Sources

The five-region calculation demonstrates a continuous family of observed behaviours: a narrow strong pulse for an axial observer, broad weak modulation for oblique observers, and nearly constant flux for a transverse observer. In this restricted sense, a resonating magnetosphere need not be recognizable as a pulsar from every direction.

The numerical example produces only **one principal peak per resonance cycle**. The second peak observed in the Crab pulsar is not reproduced here; Chapter 8 considers separate active regions, for example in northern and southern magnetospheric sectors, sharing the same global frequency but having different oscillation phases, emission spectra, and polarization signatures. A stable separation of two observed peaks would require a stable relative phase of those regions, not arbitrary uncorrelated triggering from cycle to cycle.

The present model supplies a quantitative arrival-time mapping and a reproducible light curve. Its central open physical requirements are an experimentally validated propagation law, a dynamical derivation of the prescribed κ_i from a realistic global magnetospheric mode, and an independently established radiation budget. These conditions are kept distinct from the numerical consistency of the constructed example.

8. Formation of Multiple Pulses

The numerical example in Chapter 7 showed that a single oscillating magnetospheric region can produce one pronounced maximum per oscillation period in the proposed arrival-time model. A pulsar may nevertheless exhibit two or more maxima. This chapter examines the simplest extension: two spatially distinct emitting regions, provisionally associated with the northern and southern

magnetosphere, that share one global oscillation frequency while retaining different local responses. The aim is to determine which features of a double pulse follow from the kinematic model and which require additional information about magnetospheric structure.

8.1. Independent Active Regions Within a Common Resonator

Let two emitting regions be denoted by N and S. Both are excited by a global electromagnetic mode of angular frequency ω_0, but their local velocity fields, spatial extents, emissivities, and response phases need not coincide. A minimal representation is

$$u_N(s,t) = U_N(s)\sin\big(\omega_0 t + \psi_N(s)\big),$$

$$u_S(s,t) = U_S(s)\sin\big(\omega_0 t + \psi_S(s)\big).$$

Here s is a local spatial coordinate, U_j is the velocity amplitude, and ψ_j is the local phase. The velocities are projected onto the observer's direction before being used in the arrival-time equation. The shared frequency is an explicit assumption of the coupled-resonator picture; it does not require identical pulse shapes or brightnesses.

The two regions are **dynamically coupled rather than completely independent**. The global mode can supply a common clock, while local plasma conditions select the response amplitude and phase. If pulse-producing configurations occurred at entirely random phases from cycle to cycle, their peaks would disappear in a long-time folded average. Consequently, reproducible double peaks require a sufficiently stable phase relation between the two emitting regions, although their single-pulse intensities may fluctuate.

8.2. Northern and Southern Magnetospheric Emission

For an illustrative geometry, associate region N with a northern magnetospheric volume and region S with a southern volume. These labels refer to two model regions, not to an observational identification of the emission sites of a particular pulsar. Both regions radiate toward all directions in the simplified emission assumption; the relevant difference between observers arises through the line-of-sight projections of the oscillatory velocities and the resulting arrival-time mapping.

Let $\mathbf{r}_j(s,t_e)$ and $\mathbf{v}_j(s,t_e)$ represent the emitting position and velocity. For an observer in direction $\mathbf{n}$ at large distance D, the proposed source-dependent propagation law gives the approximate arrival-time relation

$$t_{a,j} = t_e + \frac{D - \mathbf{n}\cdot\mathbf{r}_j(s,t_e)}{c + u_j(s,t_e)},$$

$$u_j = \mathbf{n}\cdot\mathbf{v}_j.$$

The sign convention is chosen so that positive u_j denotes motion toward the observer and increases the hypothesized propagation speed. The expression is conditional on the $c+u$ assumption discussed in Chapter 2 and Part C2; in standard vacuum electrodynamics source velocity does not modify the subsequent vacuum propagation speed. Any quantitative inference about pulsars based on this term remains conditional on experimental validation of that assumption.

The actual three-dimensional positions affect the geometric part of the travel time. Therefore, a separation of emission regions into northern and southern hemispheres does **not** alone imply two pulses or specify their phase separation. A

different time-dependent velocity response is required.

8.3. Phase Separation Between Two Pulses

For a transparent calculation, let each region have an effective sinusoidal line-of-sight velocity with dimensionless compression parameter k_j, and subtract the constant light-travel time. Introduce the source phase $\varphi = \omega_0 t_e$ and the arrival phase $y = \omega_0 \tau$. In the leading-order approximation the time map is

$$y = \varphi - k_j \sin\varphi, \qquad 0 \le k_j < 1.$$

Its Jacobian is

$$\frac{dy}{d\varphi} = 1 - k_j \cos\varphi.$$

A phase offset α_j in the received curve is introduced as a phenomenological parameter accounting for the region's different emission phase and geometric travel-time offset. Thus $y - \alpha_j = \varphi_j - k_j \sin\varphi_j$, with the inverse relation evaluated separately for each region. The observed flux, normalized to the *mean flux of that region*, becomes

$$g_j(y) = \frac{1}{1 - k_j \cos\varphi_j (y - \alpha_j)}.$$

In particular, the peak position is $y = \alpha_j$ for this elementary model. If the two maxima are observed at phases α_N and α_S, their separation is

$$\Delta t = \frac{T_0}{2\pi} \bmod(\alpha_S - \alpha_N, 2\pi).$$

The Crab pulsar has two prominent high-energy peaks separated by approximately 0.398 of the rotation-phase convention used to fold observations. With $T_0 = 33.5$ ms, the corresponding separation is

$$\Delta t \simeq 0.398 \times 33.5 \text{ ms} = 13.33 \text{ ms},$$

$$\Delta\alpha \simeq 2\pi \times 0.398 = 2.50 \text{ rad } (143.3^\circ).$$

This value is taken from observations; it has not been predicted from the magnetospheric dynamics. The two-region model can accommodate the separation by a suitable relative phase, but its physical origin would require a calculation of coupled spatial eigenmodes and emission-region geometry.

8.4. Different Pulse Intensities and Widths

For two incoherent emitting regions their received intensities add. Denoting the mean contribution of each region by $\overline{F}_j$, the combined profile is

$$F(y) = \overline{F}_N g_N(y) + \overline{F}_S g_S(y).$$

Each g_j has unit mean over one observed cycle, so the integrated mean flux is $\overline{F}_N + \overline{F}_S$. A pulse can be more intense because its emitting region supplies greater mean power, because its time map produces greater compression, or because both factors act together. A larger active surface may supply greater power if the emissivity per unit area and other conditions are comparable. None of these quantities follows from the phase separation alone.

For a concrete illustrative profile choose $T_0 = 33.5$ ms, $k_N = 0.88$, $k_S = 0.76$, $\alpha_N = 2\pi \times 0.090$, $\alpha_S = 2\pi \times 0.488$, and $\overline{F}_S = 0.57\overline{F}_N$. This gives maxima separated by $0.398 T_0 = 13.33$ ms before the weak mutual overlap of the two components is considered. The peak-to-mean factors of the isolated components are $(1 - k_N)^{-1} = 8.33$ and $(1 - k_S)^{-1} = 4.17$; the latter is multiplied by its smaller mean-flux weight in the combined curve.

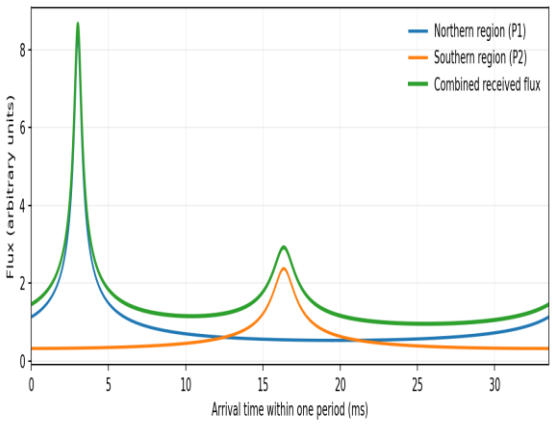


***Figure 5**. Illustrative double-pulse profile for two magnetospheric emitting regions. The main and secondary components have different arrival phases, compression parameters, and mean powers. Their total is the sum of the two received fluxes.*

Table 8.1. Parameters of the illustrative two-region profile.

Quantity	Northern region, P1	Southern region, P2
Common oscillation period	33.5 ms	33.5 ms
Compression parameter k	0.88	0.76
Phase of isolated maximum	0.090 cycles	0.488 cycles
Mean-flux weight	1.00	0.57
Isolated peak / own mean	8.33	4.17

Although the model admits unequal components, the illustrative numbers are *not* fitted to a full, frequency-resolved Crab dataset. In particular, the widths and relative heights of the measured peaks vary across radio, optical, X-ray, and gamma-ray bands. The parameters must not be treated as universal properties of the two hypothetical regions.

8.5. Spectral and Polarization Differences Between Emission Regions

Distinct emitting regions may have different plasma densities, field strengths, particle distributions, local geometries, and propagation conditions. Therefore, they need not have identical spectra or polarization. In a frequency-resolved extension of the model, the mean emitting power and effective arrival-time response could depend on the electromagnetic radiation frequency ν:

$$F_\nu(y) = \overline{F}_{N,\nu} g_{N,\nu}(y) + \overline{F}_{S,\nu} g_{S,\nu}(y).$$

A useful working hypothesis is that one component may originate closer to the neutron star, where the background magnetic field is generally stronger, while another may arise farther into the magnetosphere. A dipole estimate provides the geometrical scale

$$B(r) \propto r^{-3}.$$

However, **a stronger magnetic field does not by itself imply a harder emitted spectrum**. Spectral hardness depends on the emission mechanism and on the energy distribution of the radiating particles or fields. Consequently, associating the smaller, harder high-energy component with an inner magnetospheric region is a hypothesis to be tested, not a deduction from the dipole law.

Observations of the Crab pulsar show that its main pulse and interpulse can differ in spectral slopes and polarization, and that radio components do not map one-to-one onto high-energy components at every observing frequency. These differences are compatible with heterogeneous emission regions, but they do not uniquely locate the two sources at opposite magnetic poles. Polarization measurements offer an independent constraint on the field

orientation and propagation geometry that the present kinematic treatment does not yet calculate.

The two-region construction thus establishes a limited but useful result: one shared oscillation period can be associated with two received pulses of different phase, amplitude, and shape without requiring two separate global clocks. The separation, individual emissivities, and frequency-dependent polarization still require an independently specified magnetospheric model. Chapter 9 confronts these limitations with the observations of the Crab pulsar. **[13], [14], [16]**

9. Comparison with the Crab Pulsar

The Crab pulsar (PSR B0531+21, also catalogued as PSR J0534+2200) provides a demanding observational test for the proposed resonant-magnetosphere model. It displays a stable, short repetition period; a complex radio profile; two prominent peaks in high-energy emission; changes in spectral hardness and polarization; and strong emission extending from radio wavelengths to gamma rays. Unlike a generic illustrative pulse train, these properties impose simultaneous constraints on the model. The comparisons below distinguish **observed quantities**, **outputs of the explicitly defined model**, and **values selected to reproduce observations**.

9.1. Observed Period and Pulse Profile

A representative repetition period is approximately 33.5 ms, corresponding to approximately 29.85 Hz. The pulsar's period and period derivative depend on the observational epoch; for example, the Fermi third pulsar catalogue lists a period of 33.6509 ms and a derivative of about $4.20 \times 10^{-13}\ \mathrm{s\,s^{-1}}$ [17]. The approximately 33.5 ms value is retained throughout this chapter for consistency with Chapters 6–8, not represented as an exact contemporary ephemeris.

The radio-parallax distance is $D = 1.90^{+0.22}_{-0.18}\ \mathrm{kpc}$ [11]. A representative phase-averaged radio flux density at 1.4 GHz is $S_{1400} \simeq 14\ \mathrm{mJy}$ [1]. High-energy profiles contain two major peaks, P1 and P2, separated by $\Delta\varphi = 0.398 \pm 0.003$ cycle in Fermi-LAT observations [12]. The corresponding time interval for the representative period is

$$\Delta t_{12} = 0.398\, T_0 \simeq 13.33\ \mathrm{ms}, \qquad T_0 = 33.5\ \mathrm{ms}.$$

The complementary interval to the next main peak is about 20.17 ms. The two separations are therefore not equal. Moreover, the radio profile contains additional frequency-dependent components; P1 and P2 do not exhaust the observed radio phenomenology **[1, 13, 14]**

Observable	Representative value	Status and source
Distance	$1.90^{+0.22}_{-0.18}$ kpc	Parallax measurement [2]
Repetition period	~ 33.5 ms	Rounded working value; see epoch-dependent catalogue [1]
Radio flux density at 1.4 GHz	~ 14 mJy	Phase-averaged [1, 3]
Main high-energy	0.398 ± 0.003 cycle	Fermi-LAT [4]

Observable	Representative value	Status and source
peak separation		
Main gamma-ray peak lag relative to radio	$-281\ \mu s$	First gamma peak arrives earlier [4]
Period derivative	$\sim 4.2 \times 10^{-13}$ s s^{-}	Epoch-dependent timing [1]

9.2. Magnetospheric Dimensions and Resonance Frequency

Chapter 3 introduced a geometric, lumped-element approximation: a spherical capacitor between the stellar surface and a hypothetical outer conducting surface, coupled to a circular current loop. Taking the stellar radius as $R_* = 12$ km and the effective current-channel radius as $a = 0.01R$, the corresponding estimates are

$$L(R) = \mu_0 R \left[\ln\left(\frac{8R}{a}\right) - 2\right],$$

$$C(R) = 4\pi\varepsilon_0 \frac{R_* R}{R - R_*},$$

$$T_{\mathrm{LC}}(R) = 2\pi\sqrt{L(R)C(R)}.$$

Solving $T_{\mathrm{LC}} = 33.5$ ms yields approximately

$$R \simeq 3605\ \mathrm{km}, \quad L \simeq 21.22\ \mathrm{H}, \quad C \simeq 1.340\ \mu\mathrm{F}.$$

This is a **parameter fit**, not an independent prediction of the Crab period. The conducting outer sphere and circuit closure have not been established for a magnetospheric plasma. Furthermore, the signal travel time around a circular path of radius 3605 km is

$$t_{\mathrm{circ}} = \frac{2\pi R}{c} \simeq 75.5\ \mathrm{ms},$$

more than twice the fitted 33.5 ms period. Consequently, a conventional quasi-static single-loop LC circuit is not a self-consistent dynamical description at that scale. The physically relevant problem is a **distributed electromagnetic/plasma eigenmode** with boundary conditions, currents, wave speeds and damping determined independently. The LC calculation only identifies a potentially relevant characteristic scale.

For comparison, if the observed period represents the stellar rotation period, the corresponding standard light-cylinder radius is $R_{\mathrm{LC}} = cT_0/(2\pi) \simeq 1598$ km. The proposed model instead allows a slowly rotating star; its actual light-cylinder radius would then depend on that independently specified rotation rate. The observed repetition period alone cannot determine that radius under the proposed hypothesis. **[3]**

9.3. Observed Radio Flux and Required Emitting Power

For a transparent numerical comparison, adopt a hypothetical observing bandwidth $\Delta\nu = 100$ MHz centered near 1.4 GHz. The measured **phase-averaged** flux density is converted to a band-integrated flux using

$$\overline{F}_{\mathrm{r}} = S_{1400}\Delta\nu \simeq 1.4 \times 10^{-20}\ \mathrm{W\,m^{-2}}.$$

This is an illustrative band estimate, assuming an approximately constant spectrum within the selected bandwidth. At $D = 1.90$ kpc the isotropic-equivalent power is

$$P_{\mathrm{iso,r}} = 4\pi D^2 \overline{F}_{\mathrm{r}} \simeq 6.05 \times 10^{20}\ \mathrm{W}.$$

For a hypothetical uniformly illuminated conical beam of half-opening angle θ, its solid angle is $\Omega = 2\pi(1 - \cos\theta)$. If this **same angular region** contains the relevant

phase-averaged radiation, its beam-corrected radiated power is

$$P_{\mathrm{beam,r}} = \Omega D^2 \overline{F}_{\mathrm{r}}.$$

For $\theta = 0.1^\circ$, $\Omega \simeq 9.57 \times 10^{-6}$ sr and $P_{\mathrm{beam,r}} \simeq 4.61 \times 10^{14}$ W. This number is **conditional**, not a measurement of the Crab's emitted radio power. A narrow instantaneous beam can sweep a larger angular region over the cycle, and this changes the phase-averaged luminosity and the solid angle relevant to an energy budget.

Hypothetical half-angle	$\Omega/(4\pi)$	Band power inferred from mean flux
Isotropic	1	6.05×10^{20} W
1°	7.62×10^{-5}	4.61×10^{16} W
0.1°	7.62×10^{-7}	4.61×10^{14} W
0.01°	7.62×10^{-9}	4.61×10^{12} W

For an assumed effective on-pulse duty fraction of $\delta = 0.05$, a simple rectangular-profile approximation would imply an on-pulse flux approximately $\overline{F}_{\mathrm{r}}/\delta = 20\overline{F}_{\mathrm{r}}$, *if nearly all energy in that band arrives during the on-pulse interval*. This is a temporal concentration factor, distinct from the angular beaming correction. Neither factor independently determines the fraction of magnetospheric area that must radiate: that also requires its local emissivity and the angular/temporal radiation mapping. **[1]**

9.4. Pulse Width and Intensity

The five-region example of Chapter 7 assigns continuously emitting regions a common angular frequency $\omega_0 = 2\pi/T_0$, but different velocity amplitudes. With ϑ the angle between their oscillation axis and the observer, a representative law is

$$u_i(t) = U_i \sin(\omega_0 t), \qquad U_i = \kappa_i \frac{c^2}{D\omega_0},$$

and the radial velocity component is $u_{r,i} = u_i \cos\vartheta$. Under the **hypothesized** velocity-dependent propagation law, the arrival-time mapping for each region is

$$t_{\mathrm{a},i} = t_{\mathrm{e}} + \frac{L_i(t_{\mathrm{e}})}{c + u_{r,i}(t_{\mathrm{e}})}.$$

The transformation of continuously emitted energy is governed, in the one-to-one mapping regime and with the appropriate emitted-energy and geometrical factors, by the inverse Jacobian $\left|dt_{\mathrm{a},i}/dt_{\mathrm{e}}\right|^{-1}$. Merely making emissions from different positions arrive simultaneously does **not**, by itself, increase the flux of a stationary, continuously emitting source. Temporal compression of successive emission intervals is essential for the pulse amplification in the toy calculation.

The numerical Chapter 7 example gives an on-axis peak of approximately eight times the cycle-averaged flux and a pulse width of about 0.86 ms, with progressively weaker and broader modulation away from the oscillation axis. These values follow from **chosen** κ_i values and the propagation assumption; they are not independent predictions of the observed Crab profile. Pulse width must also be specified separately for each observing band and for each component, since radio and gamma-ray profiles are not identical.

9.5. Main Pulse and Interpulse

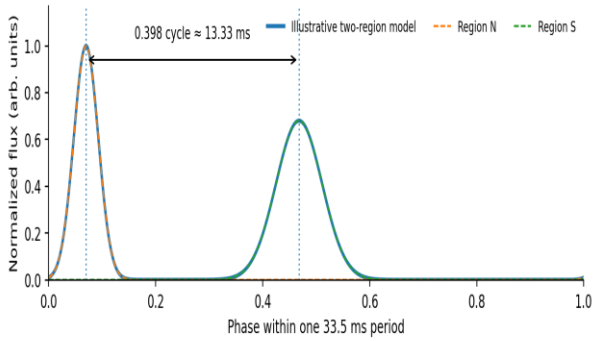
Chapter 8 explored two active magnetospheric regions (N and S), both excited by the same global resonance. Their velocity patterns may differ in

amplitude, phase and location. A minimal model writes

$$u_N(s,t) = A_N(s)\sin(\omega_0 t + \phi_N),$$

$$u_S(s,t) = A_S(s)\sin(\omega_0 t + \phi_S).$$

The received flux is the sum of the contributions from both regions, after application of each region's distinct emission-to-arrival-time mapping. A phase separation of 0.398 cycle can be **imposed** to construct a profile compatible with the observed P1–P2 spacing. It does not follow uniquely from the LC frequency, nor does it establish that the regions occupy opposite magnetic hemispheres.



Illustrative two-region light curve with the observed high-energy peak separation imposed; peak heights and widths are model choices, not measured Crab data.

Figure 6. *An illustrative sum of two periodic contributions. The separation is fixed to the observed 0.398 cycle (about 13.33 ms for the rounded reference period); individual widths and amplitudes have been chosen to demonstrate a non-identical pair of peaks. This figure must not be interpreted as an independent reconstruction of measured Crab light curves.*

The hypothesis that one pulse originates closer to the neutron star and another farther out is physically testable only if the model links emitting altitude to spectrum, arrival phase and polarization. A harder spectrum in the weaker observed pulse does not alone establish a lower emitting altitude. **[13, 15]**

9.6. Spectral and Polarization Characteristics

The emission spans radio, optical, X-ray and gamma-ray bands, with changes in profile between bands. For high-energy gamma rays, Fermi-LAT measured a systematic offset of the first gamma peak relative to the main radio peak: approximately 281 microseconds earlier [12]. This sets a cross-band timing constraint that a common resonant clock alone does not explain. Different emission sites or propagation responses must generate the observed offset.

Measurements with the LST-1 telescope found differing very-high-energy spectra for the two major peaks. Using the photon-index convention $dN/dE \propto E^{-\Gamma}$, the fitted indices were $\Gamma_1 = 3.44 \pm 0.15$ and $\Gamma_2 = 3.03 \pm 0.09$ over the applicable high-energy analysis ranges [15]. P2 is therefore spectrally harder. These values constrain any proposal that associates spectral hardness with emitting altitude or local magnetic/plasma conditions, but do not determine the altitudes by themselves.

Optical polarization studies found related but non-identical polarization-angle sweeps of the main pulse and interpulse, around 130 degrees and 100 degrees after subtraction of an approximately steady component [16]. The radio high-frequency interpulse shows a different phenomenology, including strong linear polarization and distinctive spectral bands, whereas lower-frequency main pulses exhibit highly variable nanoshot structure [13, 14]. The term *interpulse* therefore cannot be assumed to designate a single, spectrally unchanged emitting component across the whole radio band.

In the proposed model, a shared oscillation frequency is compatible with different local emission processes and polarization orientations. **[13, 14, 15, 16]**

9.7. Agreement, Discrepancies, and Unresolved Questions

The comparison with the Crab pulsar establishes several useful consistency conditions while leaving important aspects of the proposed mechanism open to independent verification. The model can reproduce a 33.5 ms repetition period by selecting an effective LC geometry, and two active magnetospheric regions can generate distinct peaks when their relative phase is prescribed. These agreements do not determine the physical eigenmode or predict the observed separation of the peaks from first principles. Future measurements and calculations should therefore focus on observables that can be evaluated independently of such fitted parameters.

A first priority is to constrain the effective spatial extent and oscillatory structure of the magnetosphere. Observations of emission-region geometry, frequency-dependent pulse heights, polarization and magnetospheric variability could be compared with the length scales inferred from the resonant model. A physically derived, distributed electromagnetic–plasma eigenmode would be required to calculate the repetition frequency and the spatial velocity pattern without choosing the resonator radius solely to match the measured period. Its damping and response to irregular excitation must also be tested against the exceptional phase stability of observed pulses.

A second group of tests concerns the predicted arrival-time concentration. At known distance and for an independently specified velocity field, the model should calculate pulse contrast, width, asymmetry and their changes with observing direction. The proposed c + u propagation law produces a characteristic dependence on source distance; comparisons across pulsars must therefore control for intrinsic emission properties and geometry rather than attributing every profile difference to propagation. The direct differential measurements proposed in Part C2 remain a separate and decisive test of this propagation assumption. [18]

Broadband observations provide further constraints. Simultaneous radio, optical, X-ray and gamma-ray timing could test whether peak phases and widths follow a common resonant cycle while allowing distinct emission regions and physical radiation mechanisms. In particular, the two principal Crab components should be examined separately for their frequency-dependent intensity ratio, spectral slopes, polarization-angle evolution and relative arrival times. The possibility that the spectrally harder component originates nearer the neutron star is a hypothesis to be evaluated through independent emission-height or magnetospheric-geometry diagnostics, not inferred from spectral hardness alone.

The energetic and kinematic interpretation also requires independent checks. Narrow concentration of radiation toward an observer can lower the total power needed for a given received pulsed flux relative to an isotropic-equivalent estimate, but this does not remove the observed energy requirements of the surrounding Crab Nebula. Conversely, the conventional rotational spin-down power is inferred from a rotation interpretation of the measured period and a stellar moment of inertia; it is not an isotropic-radiation estimate. Binary timing, astrometry and long-term pulse monitoring can help distinguish changes in arrival times caused by source motion from changes in the intrinsic resonant period.

Overall, a decisive assessment requires the joint prediction of frequency, phase coherence, pulse profile, spectral behavior and energy balance from a physically defined magnetospheric model. These measurements would establish whether resonance-driven arrival-time

concentration offers explanatory and predictive power beyond a mathematical reproduction of selected Crab-pulsar observables. [12]

10. Stellar Motion and Observed Pulse Periods

The proposed resonant model distinguishes the intrinsic period of a global magnetospheric oscillation from the interval between successive pulses received by an observer. Translational motion, orbital motion, and stellar rotation need not generate the intrinsic oscillation, although they can modify arrival times, observable phases, and—in some geometries—pulse intensities. The following relations describe kinematic propagation effects at first order in speed divided by c. They do not establish the proposed source-velocity-dependent propagation law discussed in Section 2.3.

10.1. Radial Motion Relative to the Observer

Consider a source emitting successive pulses at intrinsic intervals T_o. Let $D(t_e)$ denote the distance to the observer at the emission time t_e, and let $v_r = dD/dt_e$ be positive when the source recedes. For the conventional vacuum propagation law, the arrival time is

$$t_a = t_e + \frac{D(t_e)}{c}.$$

Differentiation yields the first-order relation between received and emitted periods:

$$T_{obs} \approx T_0\left(1 + \frac{v_r}{c}\right).$$

A uniform radial velocity therefore causes an approximately constant offset of the measured period, rather than a continuous secular drift. Approaching motion shortens the received interval; recession lengthens it. These changes do not require any variation of the magnetospheric resonance itself.

In the alternative propagation hypothesis of Section 2.3, the source-frame velocity may enter the assumed propagation speed. The arrival-time relation must then be recalculated consistently with the motion of the emission site and the distance to the observer. The ordinary Doppler expression above cannot be transferred unchanged to that hypothetical law. [18]

10.2. Orbital Motion in Binary Systems

A neutron star orbiting a companion exhibits periodic changes of its line-of-sight distance and velocity. The principal geometric effect is a varying light-travel delay. For an ideal circular orbit the first-order delay can be written as

$$\Delta t_{or\beta} = \frac{a_1 \sin i}{c} \sin(\Omega_{or\beta}\, t + \varphi_{or\beta}).$$

Here a_1 is the orbital semimajor axis of the neutron star around the barycentre, i is the orbital inclination, and $\Omega_{or\beta}$ is the orbital angular frequency. This delay modulates the phase of the observed pulses while leaving the intrinsic resonant period unchanged in the simplest model.

For an illustrative projected orbital semimajor axis of one light-second and an orbital period of one day, the arrival-time excursion has a one-second amplitude. The associated maximum line-of-sight speed is approximately 21.8 km/s. Thus orbital modulation may be readily measurable even when the global magnetospheric oscillation remains essentially unaffected. Additional changes of pulse amplitude require independent geometric or physical coupling; they do not follow from the travel-time delay alone.

10.3. Slow Rotation of the Neutron Star

The resonant mechanism developed in this work does not require that the observed pulse period coincide with the rotation period of the star. An idealized nonrotating neutron star is

therefore the baseline configuration. Slow rotation may be introduced as a perturbation, particularly if the magnetic symmetry axis and the rotation axis are not aligned.

For a star rotating with period T_{rot}, the angular displacement during one magnetospheric oscillation of intrinsic period T_0 is

$$\Delta\varphi_{\mathrm{rot}} = 2\pi \frac{T_0}{T_{\mathrm{rot}}}.$$

For T_0 = 33.5 ms and rotation periods of 1, 3 and 6 hours, the angular displacements per oscillation are approximately 0.00335°, 0.00112° and 0.000558°, respectively. These angles are small on the time scale of an individual pulse, although their cumulative effect over hours can alter the viewing geometry of an asymmetric magnetosphere.

In a corotating description, the Coriolis acceleration of a plasma element with velocity v relative to that frame is

$$\vec{a}^{\mathrm{c}} = -2\,\vec{\Omega} \times \vec{v}.$$

For a harmonic oscillation of angular frequency ω_0, the maximum order-of-magnitude ratio of Coriolis to oscillatory acceleration is $2\Omega/\omega_0$, when the velocity is perpendicular to the rotation axis. With T_0 = 33.5 ms and T_{rot} = 3 h, this ratio is about 6.2×10^{-6}. Consequently, direct Coriolis coupling is weak in this illustrative slowly rotating case, while the detailed three-dimensional mode structure and emission pattern remain to be calculated.

10.4. Changes in the Observed Pulse Period

Observed pulse-period derivatives can contain both intrinsic and kinematic contributions. If the resonance itself evolves, its intrinsic period varies with the effective inductance and capacitance of the magnetospheric mode:

$$T_0 = 2\pi\sqrt{(LC)}, \quad \frac{\dot{T}_0}{T_0} = \frac{1}{2}\left(\frac{\dot{L}}{L} + \frac{\dot{C}}{C}\right).$$

In the standard first-order propagation approximation, line-of-sight acceleration adds a kinematic contribution. For slow source motion the combined relation is

$$\frac{\dot{T}obs}{Tobs} \approx \frac{\dot{T}_0}{T_0} + \frac{a_{\mathrm{r}}}{c}.$$

The interpretation of any measured period derivative therefore requires an independent assessment of source acceleration. As an illustrative calculation, a pulse period T = 33.5 ms and period derivative $\dot{T} = 4.2 \times 10^{-13}$ s/s would correspond, if attributed entirely to radial acceleration, to $a_r \approx 3.76 \times 10^{-3}$ m/s². This numerical equivalence does not constitute evidence that the Crab pulsar experiences such an acceleration.

Transverse motion can also introduce an apparent positive period derivative (the Shklovskii effect), while gravitational acceleration along the line of sight and binary dynamics can introduce further changes. These effects are routinely considered in precision pulsar timing. They should not be conflated with changes in the internal oscillation frequency. [9]

10.5. Implications for the Resonant Model

The three types of motion have different conceptual roles. Uniform radial translation modifies the observed timing scale; orbital motion produces a periodic timing signature; and slow rotation may modify viewing geometry and weakly couple to magnetospheric oscillations. None of these motions is required to provide the fundamental periodicity in the proposed resonance-based account.

This distinction is useful when interpreting observations, but it does not remove the need to test the resonance model against independent timing constraints. In particular, the source-dependent propagation law c + u remains a separate empirical hypothesis. A consistent timing solution must specify the propagation prescription before kinematic corrections can be assigned to either source

motion or intrinsic resonance evolution. **[8, 9, 10]**

11. Discussion

The proposed model interprets pulsar periodicity as a possible consequence of global electromagnetic oscillations of a neutron-star magnetosphere, while the received pulse profile is governed by the propagation and arrival-time mapping of radiation from magnetospheric regions. The principal distinction from the conventional interpretation is not the existence of magnetospheric plasma or directional emission, both of which are well-established elements of pulsar physics, but the assignment of the pulse repetition frequency to a magnetospheric resonance rather than stellar rotation.

The preceding chapters developed three levels of description: a geometrical LC analogy for the characteristic resonant scale; a coupled global–local model for the excitation and stability of oscillations; and an explicit five-region arrival-time calculation based on the proposed velocity-dependent propagation law. These levels are not yet a closed self-consistent solution of the electromagnetic and plasma equations. Their implications, limitations, and observational tests are distinguished below.

11.1. Resonance Versus Rotation as the Origin of Pulsations

In the standard rotational framework, the periodic viewing geometry is tied to the spin of a magnetized neutron star. This framework is supported by pulsar timing, spin-down behavior, polarization geometry, and observations of accreting and binary neutron stars. The alternative examined here assigns the primary repetition period to a global oscillatory magnetospheric mode. It does not require a stationary neutron star in all cases: slow rotation may coexist with the mode and can modify its spatial orientation without necessarily setting the pulse frequency.

The distinction is observationally consequential. If the repetition period measures a resonance, the period alone is not an independent measurement of the stellar spin rate. Conversely, a resonant interpretation must still account for the extensive evidence connecting pulsar phenomenology with stellar rotation. The model therefore proposes a competing dynamical source for periodic emission; it does not establish that known neutron stars are nonrotating.

The elementary circuit representation estimated $L \approx 5.89$ H and $C \approx 1.35$ μF for an illustrative 1000-km scale, yielding $f \approx 56.4$ Hz. Such agreement in order of magnitude is informative but not an eigenfrequency calculation. At this scale, electromagnetic travel times around the presumed current path are comparable to, or exceed, an oscillation period. A distributed plasma-field eigenmode with physically justified current closure, electrical boundary conditions, and damping must ultimately replace the lumped LC approximation.

11.2. Pulsars and Weakly Modulated Neutron Stars

The arrival-time calculation in Chapter 7 yielded strongly different profiles for observers viewing the same prescribed oscillating region along different directions. With a fixed intrinsic repetition period and equal time-averaged emission per model region, the on-axis normalized peak reached approximately eight times the cycle-averaged flux, while the transverse direction exhibited no temporal modulation. Intermediate angles produced broader and less pronounced maxima. This is a model result, not a measurement of the three-dimensional emission geometry of the Crab pulsar.

The example suggests a testable selection effect: a resonantly active neutron star need not appear as an obvious pulsar to every

observer. Broad or low-contrast profiles may evade searches optimized for short duty cycles; nearly continuous emission may require sensitive searches for weak periodic structure. Known broad-profile pulsars and neutron stars with low pulsed fractions motivate this comparison, but do not by themselves support the proposed propagation mechanism.

An important limitation is that a wide observed pulse is not uniquely equivalent to a large angular beam, and a narrow pulse is not uniquely equivalent to a very small emitting surface. Temporal compression, emissivity, line-of-sight geometry, and the motion of the emitting regions must be considered separately. Observational selection should be compared with calibrated survey sensitivity before inferring an unobserved population.

11.3. Energy Requirements and Radiation Concentration

The model makes an essential distinction between the energy radiated into the observer's direction and the energy released by the source as a whole. A narrow directional distribution can greatly reduce the total power inferred from an isotropic-equivalent flux, but its reduction factor depends on the solid angle covered by the radiation over a complete cycle—not only on the instantaneous angular width of a local enhancement. Furthermore, temporal remapping changes the received power per unit arrival time while the corresponding finite emitted-energy budget must remain conserved.

$$P_iso = 4\pi D^2 F, \quad P_beam = \Omega D^2 F$$

The earlier numerical examples used assumed angular widths and effective emission powers. These estimates show that an observed radio flux can be compatible with a much smaller emitted power if the radiation is restricted to a narrow angular region; they do not measure the beaming solid angle or the fraction of magnetospheric area actually active. A quantitative emission-area estimate also requires the intrinsic energy flux per unit emitting area and the conversion efficiency into the observed frequency band.

The energy budget of the Crab Nebula is a separate constraint. Its extended synchrotron and particle emission cannot be reduced merely by assuming that the pulsed radio or gamma-ray signal is strongly concentrated toward Earth. In the standard model the measured spin period derivative yields a large spin-down power after adopting a stellar moment of inertia. That inferred rotational power would not follow from the observed pulse period alone if the latter were instead an LC resonance; nevertheless, the nebular energy supply would still require an independent physical explanation.

Consequently, a slowly rotating version of the proposed model must identify a sustainable power source—magnetic-field evolution, internal processes, accretion where relevant, or another quantitatively specified reservoir—and demonstrate that its available power and lifetime are consistent with the source and surrounding nebula. Neither resonant filtering nor radiation concentration creates energy.

11.4. Differences from the Conventional Pulsar Model

The primary differences concern what determines the period, how individual pulses form, how the source is seen from different directions, and what the pulse period reveals about stellar motion. The adopted source-dependent propagation relation is especially important: after emission, a local source-velocity component u is assumed to modify the propagation speed to c + u along the line of sight. This assumption is not part of established vacuum Maxwell electrodynamics or special relativity and is addressed as an independently testable hypothesis in Part C2.

Within that assumption, radiation from continuously emitting regions can be redistributed in arrival time according to a velocity-dependent map. Spatial alignment of arrival times from distinct regions and

compression of successive emission intervals are mathematically distinct. The first condition alone does not brighten a steady source; the second changes received power per unit time and produced the calculated light curves.

$$F_obs(t_arr) \propto \Sigma_i J_i^{-1}, \quad J_i = \partial t_arr,_i \,/\, \partial t_em$$

For a single sinusoidal emitting region in the monotonic regime, the resulting profile is periodic but need not contain two maxima. Chapter 8 obtained a double-peaked example by adding a second region with a distinct phase and emissivity. The observed Crab peak separation of approximately 0.398 cycle was an input to that example, not a consequence inferred from the global resonance. The northern–southern identification is a proposed geometrical interpretation rather than an observational determination of the emission sites.

11.5. Observational Predictions and Experimental Tests

A meaningful test must compare independently fixed model parameters with observations that were not used to set those parameters. The following program distinguishes near-term tests from more demanding astrophysical inversions.

- Propagation-law test. Part C2 proposes direct measurements of whether source motion changes the speed of subsequently propagating light in vacuum. A reproducible null result at the accuracy required by the model would directly constrain or exclude its proposed temporal-concentration mechanism; a confirmed source-velocity dependence would require a comprehensive comparison with other propagation experiments.
- Distance dependence. In the model, the velocity-dependent travel-time contribution scales approximately as D u/c^2. Thus, for otherwise similar emitting regions, the same oscillatory velocity distribution predicts markedly different pulse compression at different observer distances. Whether observed pulse widths and profiles exhibit a compatible trend—after controlling for intrinsic differences and selection effects—is a strong test.
- Viewing-angle dependence. The five-region calculation predicts that the peak-to-average contrast and pulse width vary with the line-of-sight projection of the oscillatory velocity. Independent information on geometry from polarization, binary inclination, or nebular structure could be compared with this prediction.
- Independent resonance scale. If the pulse period measures a global electromagnetic eigenmode, its frequency should follow from independently constrained magnetospheric geometry, field structure, plasma response, and boundary conditions. The present fitted LC radius is insufficient for this test.
- Pulse-pair properties. A two-region model permits different spectra, polarization profiles, widths, and amplitudes for the two maxima. It must additionally explain the stability and energy dependence of their relative phase, rather than only reproducing the measured separation by fitting a phase offset.
- Timing and long-term stability. Random excitation can maintain resonant energy while also introducing phase diffusion. The modeled mode must reproduce the observed coherent timing, secular trends, and applicable abrupt changes without relying on an unconstrained phase-reset mechanism.

These tests are not equally independent: observed flux and profile width can be reproduced by changing emissivity and velocity amplitudes, whereas a propagation-law measurement and an independently computed magnetospheric eigenfrequency would place substantially stronger restrictions on the theory.

11.6. Limitations and Open Questions

The results presented in this work are a conditional theoretical construction. Its main limitations should remain explicit when drawing conclusions:

- The postulated of propagation of electromagnetic waves in a vacuum, c + u, remains a hypothesis, although there exists a method for its empirical verification, as described in Part C2. It is, in fact, a key assumption upon which the reduction in the arrival time difference over long distances—calculated here—is based.

- The spherical capacitance and circular-loop inductance are idealized geometrical estimates. The actual magnetosphere is a spatially distributed, conducting and dispersive plasma system, not a pair of solid capacitor electrodes connected to a fixed wire loop.
- A self-consistent three-dimensional global eigenmode, including charge conservation, currents, electromagnetic stresses, plasma inertia, radiation losses and boundary conditions, has not yet been solved. The nanometre-scale velocity amplitudes in the light-curve example were prescribed, not dynamically derived.
- The adopted temporal energy-remapping rule is a simplified bookkeeping model; a complete derivation of radiation intensity, spectrum and polarization in the proposed propagation framework remains necessary.
- The Crab comparison fits the nominal repetition period through a chosen resonator scale and the double-peak separation through an assumed phase offset. Reproducing these measurements does not constitute their independent prediction.
- The model has not yet supplied an independently verified, sustained energy source for the full pulsar–nebula system, nor demonstrated the phase coherence observed in precision timing.

These limitations define a concrete research path rather than an argument to discard the hypothesis without testing it. The central near-term priorities are a laboratory test of the source-velocity propagation law; a magnetospheric eigenmode calculation with a physically closed electromagnetic energy budget; and a comparison of calculated radiation profiles with phase-resolved flux, spectral, and polarization data.

In summary, the proposed resonant framework illustrates a mathematically explicit route from continuous magnetospheric emission to observer-dependent pulsed signals under an alternative propagation assumption. Its distinction from the conventional rotational interpretation is sharp enough to motivate experimental and observational tests, but the current results should be treated as a model demonstration rather than a verified replacement of the standard pulsar theory.

12. Conclusions

This study has developed an alternative, explicitly testable description of pulsar emission in which the repetition period is associated with global electromagnetic oscillations of a neutron-star magnetosphere rather than necessarily with stellar rotation. The proposed mechanism combines a resonant magnetospheric structure, local plasma motions, and a propagation hypothesis in which the velocity of radiation toward an observer depends on the radial velocity of its emitting region. The latter hypothesis is not part of established vacuum electrodynamics and remains an essential subject for independent experimental testing.

A simplified inductive–capacitive representation was used to estimate characteristic oscillation periods from magnetospheric dimensions. For an illustrative stellar radius of 12 km and a magnetospheric current loop of radius 1000 km, the adopted geometrical assumptions yield an inductance of about 5.89 H, a spherical-capacitor estimate of about 1.35 μF, and an ideal LC frequency near 56 Hz. These quantities demonstrate a possible numerical scale, not a verified normal mode: the magnetosphere is a distributed plasma system, and a conducting spherical shell and a single lumped current loop are approximations whose physical coupling still requires derivation.

The model separates the excitation of oscillations from their periodic structure. Irregular electromagnetic disturbances originating within the star and its environment may feed energy into resonant modes, while magnetohydrodynamic motions determine the local three-dimensional response. A resonance can select a narrow frequency range from broadband excitation. Nevertheless, random forcing also introduces phase fluctuations; long-term pulsar timing stability is not established merely by the existence of a resonant peak and requires a quantitative noise and feedback model.

Within the proposed source-velocity propagation law, the arrival time of continuously emitted radiation can depend sensitively on the velocity history of each magnetospheric region. The analysis distinguishes spatial synchronization of arrivals from temporal compression of successive emissions. The first alone does not amplify an otherwise steady radiation field; a pulsed light curve requires a time-dependent arrival mapping, a time-dependent emission pattern, or both. Radiation conservation and the possibility of multiple emission times contributing to one arrival interval must be retained in any quantitative calculation.

A five-region illustrative calculation with a period of 33.5 ms produces direction-dependent pulse profiles despite constant emission by each region. The model yields a strong narrow pulse along the chosen oscillation axis, weaker and broader modulation at intermediate viewing angles, and no modulation perpendicular to that axis. The numerical amplitudes and spatial velocity pattern were selected for the demonstration rather than inferred independently from magnetospheric dynamics. Consequently, these curves establish mathematical behavior of the assumed mapping, not an observational confirmation of the proposed mechanism.

Two active magnetospheric regions, potentially associated with opposite sides of the star, offer a simple extension capable of representing a main pulse and an interpulse. The measured phase separation and differences in spectral and polarization behavior of the Crab pulsar can be incorporated by assigning distinct response phases and local emission properties to these regions. The measured separation of the two principal peaks was used as an input rather than predicted from a three-dimensional eigenmode; the identification of northern and southern emitting regions also remains hypothetical.

The comparison with the Crab pulsar emphasizes the importance of distinguishing directional radiative power from isotropic-equivalent luminosity and from estimates of rotational energy loss. A narrow observer-directed beam can require much less instantaneous radiative power than an isotropic interpretation of the same measured flux. However, the emission geometry, pulse duty cycle, available source power, and independent energetic requirements of the Crab Nebula must be evaluated separately. The present model does not yet establish a complete energy budget for the source and surrounding nebula.

The decisive tests are therefore clear. First, the source-motion propagation hypothesis should be tested through the independent differential measurements proposed in Part C2. Second, a self-consistent electromagnetic–plasma calculation must demonstrate an actual global resonant mode, its excitation and phase stability, and the resulting three-dimensional velocity field. Third, that field should predict pulse widths, viewing-angle dependence, relative peak phases, spectral behavior, and polarization without assigning those quantities from observations. Comparisons with both strongly pulsed and weakly modulated neutron stars would provide additional discriminating evidence. [18]

In conclusion, resonant magnetospheric dynamics together with the proposed arrival-time mechanism constitute a coherent framework for further quantitative investigation of pulsar-like variability without imposing rapid stellar rotation as an initial assumption. The calculations developed here identify plausible model scales and observational signatures, but the alternative cannot yet be considered an established explanation of pulsars. Its scientific value will depend on direct verification of its propagation premise and on independent predictions derived from the physics of the magnetosphere.

References

[1] Manchester, R. N., Hobbs, G. B., Teoh, A., & Hobbs, M. (2005). The Australia Telescope National Facility Pulsar Catalogue. The Astronomical Journal, 129, 1993–2006. https://doi.org/10.1086/428488

[2] Lorimer, D. R. (2008). Binary and Millisecond Pulsars. Living Reviews in Relativity, 11, 8. https://doi.org/10.12942/lrr-2008-8

[3] Gralla, S. E., & Jacobson, T. (2014). Spacetime approach to force-free magnetospheres. Monthly Notices of the Royal Astronomical Society, 445, 2500–2534. https://doi.org/10.1093/mnras/stu1690

[4] Rosa, E. B., & Grover, F. W. (1912). Formulas and tables for the calculation of mutual and self-inductance (revised). Bulletin of the Bureau of Standards, 8, 1–237. https://doi.org/10.6028/bulletin.185

[5] Grover, F. W. (1946). Inductance Calculations: Working Formulas and Tables. D. Van Nostrand Company.

[6] Chen, A. Y., Yuan, Y., & Bernardi, D. (2025). Alfvén Wave Mode Conversion in Neutron Star Magnetospheres: A Semianalytic Approach. The Astrophysical Journal, 987, 42. https://doi.org/10.3847/1538-4357/adda3b

[7] Hobbs, G., Lyne, A. G., & Kramer, M. (2010). An analysis of the timing irregularities for 366 pulsars. Monthly Notices of the Royal Astronomical Society, 402, 1027–1048. https://doi.org/10.1111/j.1365-2966.2009.15938.x

[8] Freire, P. C. C., & Wex, N. (2024). Gravity experiments with radio pulsars. Living Reviews in Relativity, 27, 5. https://doi.org/10.1007/s41114-024-00051-y

[9] Edwards, R. T., Hobbs, G. B., & Manchester, R. N. (2006). TEMPO2, a new pulsar timing package – II. The timing model and precision estimates. Monthly Notices of the Royal Astronomical Society, 372, 1549–1574. https://doi.org/10.1111/j.1365-2966.2006.10870.x

[10] Becker, W., Kramer, M., & Sesana, A. (2018). Pulsar timing and its application for navigation and gravitational wave detection. Space Science Reviews, 214,

30. https://doi.org/10.1007/s11214-017-0459-0

[11] Lin, R., van Kerkwijk, M. H., Kirsten, F., Pen, U.-L., & Deller, A. T. (2023). The Radio Parallax of the Crab Pulsar: A First VLBI Measurement Calibrated with Giant Pulses. The Astrophysical Journal, 952, 161. https://doi.org/10.3847/1538-4357/acdc98

[12] Abdo, A. A., et al. (2010). Fermi Large Area Telescope Observations of the Crab Pulsar and Nebula. The Astrophysical Journal, 708, 1254–1267. https://doi.org/10.1088/0004-637X/708/2/1254

[13] Eilek, J. A., & Hankins, T. H. (2016). Radio emission physics in the Crab pulsar. Journal of Plasma Physics, 82, 635820302. https://doi.org/10.1017/S002237781600043X

[14] Hankins, T. H., Eilek, J. A., & Jones, G. (2016). The Crab Pulsar at Centimeter Wavelengths. II. Single Pulses. The Astrophysical Journal, 833, 47. https://doi.org/10.3847/1538-4357/833/1/47

[15] Abe, K., et al. (LST Collaboration). (2024). A detailed study of the very high-energy Crab pulsar emission with the LST-1. Astronomy & Astrophysics, 690, A167. https://doi.org/10.1051/0004-6361/202450059

[16] Słowikowska, A., Kanbach, G., Kramer, M., & Stefanescu, A. (2009). Optical polarization of the Crab pulsar: precision measurements and comparison to the radio emission. Monthly Notices of the Royal Astronomical Society, 397, 103–123. https://doi.org/10.1111/j.1365-2966.2009.14935.x

[17] Fermi Science Support Center. Third Fermi Large Area Telescope Catalog of Gamma-ray Pulsars (3PC), PSR J0534+2200 entry. https://fermi.gsfc.nasa.gov/ssc/data/access/lat/3rd_PSR_catalog/3PC_HTML/J0534%2B2200.html

[18] Rozman, F. (2026). Part C2 – Differential Measurement of the Propagation Velocity of Astronomical Light. Unpublished manuscript, Unified Electromagnetic Theory of Matter and Light, Section C.